Icarus 426 (2025) 116343

Contents lists available at ScienceDirect

Icarus

journal homepage: www.elsevier.com/locate/icarus

Research Paper

Expected constraints on Phobos interior from the MMX gravity and rotation observations

Alfonso Caldiero *, Sébastien Le Maistre

Earth and Life Institute, Université Catholique de Louvain, Place Louis Pasteur 3, Louvain-La-Neuve, 1348, Belgium
Reference Systems and Planetology, Royal Observatory of Belgium, 3 Avenue Circulaire, Uccle, 1180, Belgium

A R T I C L E I N F O

Dataset link: https://gitlab-as.oma.be/sbm/gila

Keywords:
Small solar system bodies
Gravitational fields
Libration
Phobos interiors
Inverse problems

A B S T R A C T

The origin of the Martian moons is still uncertain, and knowledge about their interior could provide support to some of its leading theories. In preparation for the JAXA Martian Moons eXploration (MMX) mission, we review our current knowledge on the interior of Phobos, and provide synthetic tests showing how the gravity and rotation determination could allow the detection of specific interior-structure properties. The inversion of the geodetic observables for the retrieval of the internal mass distribution of a set of synthetic interior models is performed via non-linear least-squares, where the interior parameterization is based on the level-set method. We additionally provide simple expressions allowing to relate some of these interior models to the geodetic observables of Phobos. The results, based on realistic measurement resolution and noise scenarios, show good retrievals for most of the models at the data resolutions expected from MMX. Specifically, we find the gravity information is realistically sufficient for the detection of mass anomalies below the Stickney crater, as well as large scale heterogeneous regions within plausible rubble-pile structures. Libration helps retrieve the more degenerate models for gravity, such as those with concentric layers or with density varying linearly with depth. The incremental improvement from further adding a hypothetical mean obliquity measurement is marginal. Finally, we apply the level-set inversion and the analytical formulas to estimate possible interior characteristics of the 'real' Phobos from the currently-available scarce geodetic observables. The level-set solutions for the real-data inversion generally converge to a higher mass concentration towards the surface in the equatorial region. Markov chain Monte Carlo estimations of parameters relative to a simple 2-layer model or a radial density distribution similarly hint at a lighter region inside of Phobos.

1. Introduction

Phobos, the larger and inner of the two Martian moons, is an irregularly-shaped body of modest size, with a mean radius of about 11 km. Its surface is heavily cratered and characterized by prominent features such as grooves and, most notably, the 9-km Stickney crater (Willner et al., 2014). Such characteristics make the study of this moon closely related to that of other small Solar System bodies, like asteroids and comets. As a matter of fact, one of the leading hypotheses of the formation of the Martian moons sees them as (possibly D-type) asteroids captured from the outer regions of the main belt (Burns, 1992; Murchie, 1999; Rivkin et al., 2002; Rosenblatt, 2011; Pajola et al., 2013). However, the origin of the two moons is still debated (see Rosenblatt et al., 2020; Ramsley and Head, 2021; Kuramoto, 2024, for recent reviews on the topic). The capture scenario is supported by the similarity between the reflectance spectra of their surfaces (considerably darker than Mars) and those of D-type asteroids (Pajola et al., 2013). On the other hand, as asteroids encounters with Mars are expected to happen at random directions, very specific conditions are required to justify the present low inclination and eccentricity of the two orbits (Rosenblatt, 2011), such as high dissipation inside the moons (Lambeck, 1979), aerobraking from an extended primordial Mars atmosphere (Hunten, 1979), or fortuitous initial orientations. The near-circular and near-equatorial orbits would suggest instead that the moons formed in orbit around Mars. Mechanisms that could explain an *in-situ* formation primarily involve condensation from a circum-Martian ring, be it the one accompanying the formation of Mars (Rosenblatt, 2011) or one generated by a large impact on Mars (Craddock, 2011; Rosenblatt, 2011; Citron et al., 2015; Rosenblatt et al., 2016; Hyodo et al., 2017; Canup and Salmon, 2018; Hu et al., 2020). An ancestral parent body (itself possibly formed *in-situ*) being split in two (Bagheri et al., 2021) or material released by the (partial) tidal disruption of an unbound asteroid (Kegerreis et al., 2024) could also have lead to the

* Corresponding author at: Earth and Life Institute, Université Catholique de Louvain, Place Louis Pasteur 3, Louvain-La-Neuve, 1348, Belgium
E-mail address: alfonso.caldiero@oma.be (A. Caldiero).

https://doi.org/10.1016/j.icarus.2024.116343
Received 25 June 2024; Received in revised form 23 September 2024; Accepted 11 October 2024
Available online 21 October 2024

formation of the two Martian moons. Direct co-accretion with Mars is harder to justify, given the disagreement between the spectra of the bodies (Murchie et al., 2015), and the much younger age expected for Phobos from its surface features and its current rate of orbital evolution, which should lead to its demise by tidal breakup or Mars collision in 20 to 70 Myr (Black and Mittal, 2015). Nonetheless, the moon itself may be a second-generation object, formed for instance as part of a tidally-driven cyclic ring-satellite process (Hesselbrock and Minton, 2017). Both co-accretion and martian-impact formation scenarios would lead to highly porous moons (Rosenblatt, 2011). However, for the impact scenario, the high temperatures involved should have depleted the body of volatiles (Canup and Salmon, 2018), leaving little to no water ice (Kamada et al., 2024).

Therefore, information on the interior structure of Phobos could provide additional support to any of these scenarios: detecting significant quantities of water ice inside the moon may favor the captured asteroid or co-accretion hypotheses, while a dry rubble-pile with small elemental blocks might suggest a giant impact origin or the capture of a water-poor asteroid (Ramsley and Head, 2021; Kamada et al., 2024). Furthermore, knowledge on the interior of Phobos could shed light on its past and future orbital evolution: a highly porous body with little cohesion, or with a large volatiles content, will be subject to faster orbital changes due to tidal dissipation (Lambeck, 1979; Yoder, 1982). So, for example, if at its formation the orbit of Phobos was more elliptical than it is today, as in the model of Bagheri et al. (2021), then a rubble-pile structure would imply a younger age, compared to a monolithic body.

Over the years, radio-tracking data from the Viking orbiters (Christensen et al., 1977), from Phobos 2 (Kolyuka et al., 1990), and 20 years later from the ESA Mars Express (MEX) orbiter in its flybys of the moon (Andert et al., 2010; Yang et al., 2019), have allowed to constrain the mass of Phobos to increasingly-high precision. The current estimate for the mass, coupled with the shape model of Willner et al. (2014), reveals a bulk density of $(1846 \pm 11)\,\mathrm{kg/m^3}$ (Yang et al., 2019). While no reliable analogue has yet been found for Phobos (Poggiali et al., 2022; Wargnier et al., 2023), this density is lower than that of most meteorites, suggesting the presence of ice and/or voids inside the moon (Andert et al., 2010). However, the mass by itself is not sufficient to constrain the ice/voids ratio and their spatial distributions. The extended gravitational potential of a body, being a direct expression of its distribution of mass, can be used to probe its interior. For Phobos, the degree-2 coefficients of the spherical-harmonics expansion of the gravitational potential were estimated from MEX radio-tracking data (Pätzold et al., 2014; Yang et al., 2019) and from astrometric observations (Jacobson and Lainey, 2014).

Future missions like the Martian Moons eXploration (MMX) by the Japan Aerospace Exploration Agency (JAXA) (Kuramoto et al., 2022) will target Phobos directly, and could provide the Phobos gravity coefficients with improved accuracy (Matsumoto et al., 2021).

The degree-2 coefficients estimated from MEX flybys are suggestive of a non-homogeneous interior with a denser region at the equator or a lighter region at the poles (Yang et al., 2019). Unfortunately, further interpretation of the gravity measurements is hampered by the problem being notoriously ill-posed and limited in spatial resolution. Additional observations can mitigate this issue. The non-zero eccentricity of the moon's orbit and its synchronous resonance with the spin rate give rise to a librational motion (Rambaux et al., 2012), whose amplitude is itself dependent on the mass distribution of the body, and results in an additional observable that can be used to constrain the interior. The moments of inertia of the satellite also find expression in the value of its mean obliquity (Rambaux et al., 2012). Le Maistre et al. (2019) computed the signature of various plausible Phobos interior models on some of these geodetic measurements: under realistic assumptions for the precision of the observables, the effect of specific heterogeneous mass distributions on the observables is large enough to allow discerning certain classes of interior models from others.

The present study complements the findings of Le Maistre et al. (2019). Instead of a forward approach, here we test the ability to distinguish between different patterns of interior mass distributions in the frame of the inverse approach of Caldiero and Le Maistre (2024), described in Section 3, as a function of the accuracy and resolution of the geodetic measurements mentioned above, and further described in Section 2. The results are shown in Section 4 for synthetic test cases representative of various interior distributions. The approach is finally applied to real observations in Section 5.

2. Geodetic observables

In this study, we exclusively focus on the ability of gravity and rotation to jointly constrain the interior of Phobos. In addition to the observables considered by Le Maistre et al. (2019), namely gravity and libration, here the mean obliquity is also taken into account. The different geodetic observables are described below. How and which additional observations could be introduced into the density estimation, to further restrict the range of possible solutions, is discussed in Section 3.2.2.

2.1. Gravity

The gravitational potential of the body is assumed to be available in the form of its normalized spherical harmonics (Stokes) coefficients, which are related to the interior density of the body via the integral (e.g. Jekeli, 2007):

$$\begin{bmatrix} C_{lm} \\ S_{lm} \end{bmatrix} = \frac{1}{(2l+1)\mathcal{M}} \int_{\mathcal{V}} \rho\,(r,\theta,\phi) \left(\frac{r}{r_0}\right)^l \cdot P_{lm}(\cos\theta) \begin{bmatrix} \cos(m\phi) \\ \sin(m\phi) \end{bmatrix} dV, \tag{1}$$

where $\mathcal{M}$ is the total mass of the body and $\mathcal{V}$ its total volume (dV being the volume element). Inside the integral, r_0 is a reference radius, (r,θ,ϕ) the spherical coordinates (radius, colatitude, longitude), P_{lm} the (associated) fully-normalized Legendre polynomials of degree l and order m, and C_{lm} and S_{lm} the dimensionless fully-normalized Stokes coefficients. We will use the symbol $\mathcal{O}_{lm}$ to indicate any of C_{lm} or S_{lm} wherever an expression holds for both sets of coefficients. The P_{lm} functions and $\mathcal{O}_{lm}$ coefficients are obtained from their unnormalized counterparts by respectively multiplying and dividing by the normalization factor $\sqrt{(2-\delta_{m,0})(2l+1)(l-m)!/(l+m)!}$, $\delta_{m,0}$ being the Kronecker delta.

We model the uncertainty in the gravity coefficients via the empirical curve (Tricarico, 2013):

$$\sigma(l) = \alpha 10^{\beta(l-l_{\max})} \sqrt{\frac{\sum_{m=0}^{l_{\max}} C^2_{l_{\max},m} + S^2_{l_{\max},m}}{2l_{\max}+1}}, \tag{2}$$

The parameter α is the fraction of noise relative to the root-mean-square (RMS) of the central values of the coefficients for $l = l_{\max}$, a ratio that gets propagated to lower degrees via a power law with a given logarithmic slope β. The science requirement of the MMX mission include a 2%–3% accuracy on the degree-2 gravity coefficients C_{20} and C_{22} (Matsumoto et al., 2021). Here, we generate realistic error spectra by assuming, as nominal settings in Eq. (2), $l_{\max} = 4$, $\alpha = 0.1$ (10% noise at degree-4) and $\beta = 1/3$, which is typically the slope associated to errors from small-bodies radio-science estimates (see Tricarico, 2013; Caldiero and Le Maistre, 2024). This leads to an uncertainty on the degree-2 coefficients about 10 times lower than the upper limit set by the mission requirements, but provides error spectra in agreement with the best-case predictions from radio-science simulations, according to which MMX should measure the gravity coefficients of Phobos up to degree 4 (Martinelli, 2020; Ciccarelli and Baresi, 2024), or even 5 (Yamamoto et al., 2024), depending on the actual altitude and inclination of the tracked orbits. The nominal MMX mission design consists of planar quasi-satellite orbits (QSOs) at different altitudes, approximately contained in the equatorial plane of Phobos. However, the gravity resolution mentioned above relies on the realization of at

Table 1
Published values of the low-degree gravity and the libration amplitude of Phobos. The gravity coefficients are normalized, and relative to a reference radius of 10 993 km.

Gravity		
	Pätzold et al. (2014)	Yang et al. (2019)
GM (10^5 m^3/s^2)	7.084 ± 0.002433	7.0765 ± 0.0025
C_{20}	-0.05382 ± 0.02281	-0.06163 ± 0.005188
C_{22}	0.004071 ± 0.003039	0.02572 ± 0.007901
Data	Doppler, 2010 MEX flyby	Doppler, 2010 and 2013 MEX flybys
Libration		
	Burmeister et al. (2018)	Lainey et al. (2021)
θ (°)	1.143 ± 0.025	1.09 ± 0.01
Data	Viking and MEX images	Astrometric observations

least one mission phase where the spacecraft orbit has an out-of-plane component (3D-QSO), thus presenting a large inclination angle with respect to Phobos equatorial plane (Matsumoto et al., 2021). The effect of the addition of 3D orbits to the planar ones is substantial, as they allow to additionally detect zonal and tesseral coefficients ($m < l$). Conversely, as shown in Yamamoto et al. (2024), using exclusively planar QSOs, the only coefficients that can be estimated with statistical significance are C_{20} (still assuming a small inclination of the nominal orbit) and the sectorial ($l = m$) coefficients (up to degree 3 or 7, depending on the altitude of the tracked orbits). By taking $l_{\max} = 4$, we here assume that 3D-QSOs, not nominal at the moment (Yamamoto et al., 2024), will be available.

The degree-2 coefficients of the gravity field of Phobos have been measured from Mars Express flybys by Pätzold et al. (2014), and more recently by Yang et al. (2019), as reported in Table 1. We also present below simulation tests where the number of coefficients and their associated uncertainties are derived from these measured data, instead of Eq. (2).

2.2. Libration amplitude

The non-linear differential equations describing the rotational motion of a body in synchronous spin–orbit resonance like Phobos can be linearized, providing a good first-order approximation for the libration angle. The amplitude of the main libration in longitude (i.e. forced libration at orbital period) resulting from the Fourier decomposition of this angle is related to the moments of inertia of the body via the formula (e.g. Willner et al., 2010):

$$\theta = \frac{2e}{1 - \frac{1}{3\gamma}}, \quad \text{where} \quad \gamma = \frac{\mathcal{B} - \mathcal{A}}{\mathcal{C}}, \tag{3}$$

with $e = 0.01511$ the orbital eccentricity of Phobos. Strictly speaking, $\mathcal{A}, \mathcal{B}$, and $\mathcal{C}$ are the principal moments of inertia of the body. Here, we approximate them with the terms on the main diagonal of the inertia tensor in the shape frame (that is, I_{xx}, I_{yy}, I_{zz}), since, even for heterogeneous interiors, these terms are orders of magnitude larger than the off-diagonal terms.

The most recent estimates of the libration amplitude were obtained by Burmeister et al. (2018) and by Lainey et al. (2021), respectively from photogrammetric and astrometric observations. Their corresponding values, reported in Table 1, are inconsistent at 1σ ($\simeq$1%–2%). The MMX mission is expected to measure the libration amplitude of Phobos with a roughly similar precision of 2%–3% (Matsumoto et al., 2021), possibly helping resolve this ambiguity.

2.3. Mean obliquity

The mean obliquity η can be expressed as (e.g. Eq. 11 in Rambaux et al., 2012):

$$\frac{\mu}{n} \sin(\eta - i) = -\frac{3}{2} \sin \eta \left[\frac{\mathcal{C} - \mathcal{A}}{\mathcal{C}} \cos \eta + \frac{1}{4} \frac{\mathcal{B} - \mathcal{A}}{\mathcal{C}} \sin (\eta/2)^2 \right] \tag{4}$$

with i, μ, n the orbital inclination, nodal precession, and mean motion of Phobos, respectively. For small values of the obliquity, Eq. (4) can be linearized around $\eta = 0$ to give (Baland et al., 2011):

$$\eta = \frac{i\mu}{\mu + \frac{3}{2} n \frac{\mathcal{C} - \mathcal{A}}{\mathcal{C}}} \tag{5}$$

Here the triaxiality information disappears. Yet, even for heterogeneous models, the difference coming from using either of the two equations is less than 0.1%. We therefore use the linearized expression in the following.

As mentioned in Rambaux et al. (2012), the mean obliquity of Phobos is expected to be small (3.5 arcsec), and its measurement is complicated by large (165 arcsec) oscillations due to perturbations on the orbit. Therefore, in order to precisely estimate the mean obliquity of Phobos, these perturbations (unless correctly modeled) would need to be accurately determined, which would imply an observation campaign spanning at least the full precession period of Phobos orbit, or about 2.3 years. The MMX spacecraft will in fact stay in the Martian system for 3 years, thus offering a chance to better constrain the obliquity of Phobos. Predictions for the precision on the mean obliquity achievable via MMX orbit determination are not available in the literature, as obliquity is generally fixed in the published radio science simulations (Matsumoto et al., 2021; Yamamoto et al., 2024). Still, it is very unlikely that the obliquity will be determined at the level of precision needed to further constrain the interior structure of Phobos. Indeed, one can reasonably expect its resulting uncertainty to be on the same level as that on the libration amplitude, itself realistically expected to be in the order of 0.01°. Even if a focused study using image data (such as in Burmeister et al., 2018, currently providing the pole orientation with a precision of 0.02°) were carried out, it would probably still be very challenging to reduce the uncertainty on the mean obliquity of Phobos to 1% (or 1e−5° = 0.036 arcsec, same relative uncertainty as for libration). Nevertheless, even assuming such an unrealistic level to be reachable by MMX, we find that, in our approach, this would provide only marginal reduction of the range of possible models, as discussed below.

3. Methods

The forward modeling and density estimation are performed using GILA, a Python/C++ tool designed for the global gravity inversion of small bodies and based on the level-set method as applied to Earth local-gravity inversion (Giraud et al., 2021; Li et al., 2017). For the present study, GILA has been upgraded to enable joint inversion of gravity and rotation data. In the following, we give a brief overview of the method, and refer to Caldiero and Le Maistre (2024) for a more detailed description.

3.1. Forward model

The interior of the body is discretized by a uniform hexahedral grid, which is fully contained within the polyhedral mesh representing the external shape of the moon (assumed to be known). The whole body is assigned a background density ρ_0, but each grid element might have a non-zero, uniform density contrast $\Delta\rho$, so that its density is $\rho_0 + \Delta\rho$.

In our approach, the number of different density contrasts within the body is limited to a finite value M (a parameter of the model), making the density inside the body composed of a few areas of uniform density contrast (*density anomalies*) dispersed in a uniform background material. The number of resulting anomalies is $\geq M$, as areas of equal density contrast might not be connected. The shapes of these anomalies are modeled as 0-level-sets of 3D scalar fields (or level-set functions) $\phi : \mathbb{R}^3 \mapsto \mathbb{R}$, one for each of the M possible density contrasts. Denoting with $\boldsymbol{x}$ a point in $\mathbb{R}^3$, independently of the coordinate system, the density function can then be written as:

$$\rho(\boldsymbol{x}) = \rho_0 + \sum_{j=1}^{M} \Delta\rho_j H(\phi_j(\boldsymbol{x})) \tag{6}$$

Table 2
Homogeneous geodetic observables for 3 shape models of Phobos. The gravity coefficients, normalized moments of inertia, and libration amplitudes are computed in the principal-axes frame, for a reference radius $r_0 = 10\,993$ m. The center of mass (CM) coordinates are in the original shape reference frame, hence computed before centering the shape. Cell colors in the last two columns indicate the relative difference with respect to the Willner et al. (2014) values of the first column, respectively $\leq 1\%$, $\leq 20\%$, and $> 20\%$ from lighter to darker.

	Willner et al. (2014)	Ernst et al. (2023)	Chen et al. (2024)
Volume (m^3)	5.741 18 $\times 10^{12}$	5.694 89 $\times 10^{12}$	5.740 30 $\times 10^{12}$
C_{20}	−0.047 509 8	−0.047 819 1	−0.047 900 5
C_{22}	0.025 629 3	0.024 143	0.023 936 8
x_{CM} (m)	−305.106	−82.2426	64.2361
y_{CM} (m)	−381.117	−521.556	−58.7082
z_{CM} (m)	117.127	31.4711	−84.27
$\mathcal{A}/(\mathcal{M}r_0^2)$	0.360 437	0.360 185	0.362 237
$\mathcal{B}/(\mathcal{M}r_0^2)$	0.426 612	0.422 523	0.424 041
$\mathcal{C}/(\mathcal{M}r_0^2)$	0.499 76	0.498 281	0.500 248
θ (deg)	−1.1411	−1.040 27	−1.019 72

where $\Delta\rho_j$ is one of the M different density contrasts and ϕ_j its corresponding level-set function. The Heaviside function H is 1 if $\phi_j(\boldsymbol{x}) \geq 0$ (inside the anomaly) and 0 otherwise, so that the points where $\phi_j(\boldsymbol{x}) = 0$ trace the boundaries of the anomalies of density contrast $\Delta\rho_j$. Thus, the shapes of the anomalies can be modified by perturbing the level-set functions. Following the discretization of the interior, the functions ϕ_j are evaluated at the grid nodes, corresponding to the center of each grid element.

The generic Stokes coefficient $\mathcal{O}_{lm}$ of the discretized Phobos is written as:

$$\mathcal{O}_{lm} = \frac{1}{\mathcal{M}}\left[\rho_0 \mathcal{V}\mathcal{O}_{lm}^{CD} + \sum_{i=1}^{N} \Delta\rho(\boldsymbol{x}_i)\mathcal{V}_i\mathcal{O}_{lm}^{i}\right] \tag{7}$$

where N is the total number of grid cells, $\mathcal{V}_i$ the volume of the ith cell, and $\boldsymbol{x}_i = (x_i, y_i, z_i)$ are the coordinates of its center. The term $\mathcal{O}_{lm}^{CD}$ is the homogeneous (CD stands for "constant density") Stokes coefficient of the whole body, while $\mathcal{O}_{lm}^{i}$ is the coefficient of the ith discretization element, which has a uniform density contrast $\Delta\rho(\boldsymbol{x}_i) = \rho(\boldsymbol{x}_i) - \rho_0 = \sum_{j=1}^{M} \Delta\rho_j H(\phi_j(\boldsymbol{x}_i))$ (see Eq. (6)). The Stokes coefficients appearing in Eq. (7) are here all computed using the line-integral approach of Jamet and Tsoulis (2020).

The total inertia tensor of the body (and thus the terms appearing in the libration and obliquity formulas) can be computed similarly to Eq. (7) by summing the contribution of each discretizing element (see Le Maistre et al., 2019). These contributions are all computed by numerical quadrature of a surface integral over the polyhedral meshes representing the surface and the grid elements, after application of the divergence theorem.

3.1.1. Homogeneous observables

In the following, we assume that the shape model is known. For the density estimation, inaccuracies in the shape model effectively act like biases on the input measurements. We try to quantify the level of this error by comparing the homogeneous geodetic observables for the different available shape models of Phobos, from Willner et al. (2014), Ernst et al. (2023), and Chen et al. (2024). While after centering and rotating to the principal-axes frames (Takahashi et al., 2017) the models provide compatible homogeneous gravity coefficients and normalized moments of inertia, their corresponding libration amplitudes are not in agreement (Table 2). We will adopt the shape model of Willner et al. (2014) in the following, as its libration amplitude is in better agreement with the measured values[1] (Table 1). MMX is also expected to provide an updated Phobos shape model (Matsumoto et al., 2021), which should then be the baseline when interpreting the MMX geodetic measurements.

[1] As expected, since both Burmeister et al. (2018) and Lainey et al. (2021) used this shape model.

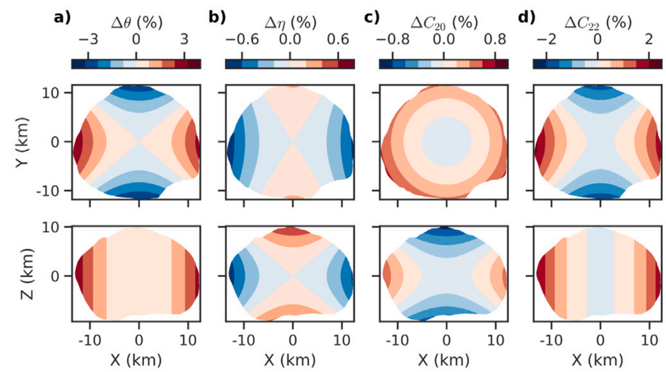

Fig. 1. Relative deviation from the homogeneous value of libration amplitude (a), obliquity (b), C_{20} (c), and C_{22} (d) due to a point-mass anomaly ($\Delta\mathcal{M}/\mathcal{M} = 0.1\,\%$), as a function of its position within Phobos and over the $z = 0$ (top) and $y = 0$ (bottom) planes.

3.1.2. Heterogeneous signature

Given the non-uniqueness of the gravity inversion problem (see Section 3.2), it is generally of interest to test known and plausible density distributions against the observations, in order to inform the exploration of the solution space of a more general density estimation approach (as done for Bennu by Scheeres et al., 2020). Here we study the signature on the observables associated to simple density anomalies inside a body. We provide here the main conclusions of a longer discussion in Appendix A, where we derive formulas for the signature of a point mass, multiple heterogeneous layers, and a radial density gradient. Fig. 1 shows the relative signature on the geodetic observables due to a point mass (excess mass of 0.1 %), as a function of its position over the $z = 0$ plane (Phobos equatorial plane) and the $y = 0$ plane. A higher concentration of mass along the y-axis (x-axis) corresponds to a decrease (increase) in the magnitude of the libration amplitude (θ) and the gravity coefficient C_{22}. The opposite behavior is observed for the mean obliquity (η), which also increases for a concentration of mass along the z-axis, whereas θ and C_{22} are independent of the position of the point mass along z. The C_{20} plots reflect the well-known behavior of the coefficient, which increases (in magnitude) when mass is added at the equator or is removed at the poles.

Any model with multiple spherical layers can be approximated by a 2-layer model that provides the same geodetic observables. If instead the layers have the same shape as the surface of Phobos (in the following, and based on Guo et al. (2021), referred to as *homothetic* layers), the libration amplitude and the mean obliquity are those of the homogeneous model. For a single homothetic core of scale factor s_c (ratio of its maximum radius and that of the external shape) and density contrast $\Delta\rho_c$, the signature ($\Delta\mathcal{O}_{lm} = O_{lm} - O^{CD}_{lm}$) on the gravity coefficient of degree l and order m ccan be computed as:

$$\Delta\mathcal{O}_{lm} = \frac{\Delta\rho_c s_c^3 (s_c^l - 1)}{\rho_{CD}} \mathcal{O}^{CD}_{lm}. \tag{8}$$

Similarly, for a density varying linearly from ρ_0 at the surface to $\rho_0 + k$ at the center, the signature on the libration amplitude and the obliquity is null, while that on the gravity coefficients is given by:

$$\Delta\mathcal{O}_{lm} = -\frac{\mathcal{O}^{CD}_{lm}}{\rho_{CD}} \frac{kl}{4(l+4)} \tag{9}$$

Eqs. (8) and (9) allow to easily check for the presence of a homothetic core or a linear radial density variation within the body. The parameters in these formulas can be estimated via classical regression methods. These expressions can additionally be combined with similar analytical formulas for simple density distributions (Takahashi and Scheeres, 2014; Scheeres et al., 2020) in order to improve the data fit. Compared to the GILA inversion method presented below, this approach is less affected by the non-uniqueness of the problem, but relies on strong assumptions on the model to retrieve. As in Scheeres et al. (2020), the analytical approach can drive the interpretation of the results of the more generic inversion. Moreover, these formulas specifically can complement the density estimation from GILA, which typically struggles to retrieve layered models due to their degeneracy. Therefore, in the real-data processing of Section 5, we will combine the GILA inversion with the estimation of layered models and radial density gradients.

3.2. GILA inversion method

In order to produce a density distribution in agreement with the data, the nodal values of the level-set functions are adjusted in an iterative least-squares inversion, together with their corresponding density contrasts and the background density. At each iteration of the Gauss–Newton algorithm, the quadratic cost function to minimize is:

$$\Psi(\boldsymbol{\delta t}) = \|\boldsymbol{y} - \boldsymbol{J}\boldsymbol{\delta t}\|_2^2 + \lambda^2\|\boldsymbol{\delta t}\|_2^2 + \Psi_c(\boldsymbol{\delta t}) \tag{10}$$

The first term on the right hand side is the data misfit, where $\boldsymbol{y}$ is the $P \times 1$ vector of residuals (difference between the observed quantities and those predicted by the current state of the model), $\boldsymbol{\delta t}$ is the $K \times 1$ vector of corrections for the model parameters, and $\boldsymbol{J}$ is the $P \times K$ Jacobian matrix of the partials relating the measurements to the model parameters in the linearized problem. The vector of K parameters, $\boldsymbol{t}$, includes the values of the level-set function in the vicinity of the boundary of each anomaly (*narrow band*) and the M density contrasts, as well as the background density ρ_0. The second term in the cost function is the classical Tikhonov regularization term, which minimizes the total norm of the corrections and is needed to stabilize the ill-posed problem. The last term, $\Psi_c(\boldsymbol{\delta t})$, is a generic set of quadratic constraints, which might be derived from observational or theoretical considerations and can be used to drive the system towards specific solutions. The partial derivatives in the matrix $\boldsymbol{J}$ are obtained via the chain rule.

3.2.1. Exploration of the solution space

The level-set formalism, while reducing the range of possible solutions, introduces non-linearity in the inversion. Consequently, for an exploration of the solution space, the iterative least-squares inversion is here usually repeated multiple times, starting from different initial models and perturbing the measurements according to their uncertainty. As in Caldiero and Le Maistre (2024), depending on the degree of similarity among the various estimated density distributions, the resulting set of solutions is further subdivided into clusters of density maps sharing common features, via k-means clustering. For each cluster of solutions and each grid element there is then a distribution of density ρ (its values across all solutions), that can be characterized in terms of its mean and standard deviation (σ_ρ, assumed to represent the uncertainty on the estimated densities). The element-wise mean density is here taken as a representative density solution for the cluster. In the average model, the background density ρ_0 is defined as the median value over all elements. Then, as in Dinsmore and de Wit (2023), the density contrasts in the average model ($\Delta\rho = \rho - \rho_0$) are divided by the density uncertainty (σ_ρ) to define their statistical significance. Values of this ratio lower than 1 would therefore indicate a detected density contrast which is consistent with 0.

3.2.2. Possible observational constraints

Gravity inversion is an ill-posed problem. The regularization, coming from the assumption of anomalies of uniform density and from the inclusion of the libration and mean obliquity information, still does not preclude ambiguity in the estimated density distributions, where multiple solutions can fit the data at the same level. Interpretation of a given density distribution in terms of porosity or ice content is itself ambiguous, and requires assumptions that go beyond the simple data fitting. It is essential, therefore, to include in the gravity interpretation information coming from other observations. These additional constrains can come in various forms. In the frame of MMX, the surface and subsurface composition, as provided by the analysis of the samples (Usui et al., 2020) and the gamma-ray spectrometer measurements (Hirata et al., 2024), could lead to constraints on the material density within the body: coupled with a density distribution, it could then provide ranges for the spatial distribution of macro-porosity and ice. Measurements of the magnitude and location of the maximum tidal deformation can provide information on the interior (Dmitrovskii et al., 2022). The phase lag of the tidal bulge, inversely proportional to the tidal quality factor Q (Murray and Dermott, 2000), is a measure of the dissipation within the body, which if high (low Q) might indicate a considerable presence of volatiles. For a future mission, the tidal effects could be measured by tracking a lander on Phobos (Le Maistre et al., 2013; Dirkx et al., 2014). Always in the frame of a hypothetical future mission, additional observations that could break the degeneracy of the gravity inversion could also come from radar or seismic tomography (Herique et al., 2018; DellaGiustina et al., 2024). Where such observations are not suitable for inclusion in the linearized approach, they can always be input as direct constraints on the level-set functions (Rashidifard et al., 2021), via the $\Psi_c(\boldsymbol{\delta t})$ term in Eq. (10).

4. Synthetic interior retrievals

Given the limited observational constraints and its irregular shape and prominent surface features, different kinds of models have been proposed for the interior of Phobos. For the purpose of this study and in line with Le Maistre et al. (2019), we classify the proposed interior models into four main groups, namely: homogeneous, rubble-pile, Stickney, and layered. The four families are presented in Fig. 2 and described in the following sections. This categorization is mainly based on the spatial scale and distribution of the heterogeneity within the body, although it is inevitably related to specific scenarios in the origin and evolution of Phobos, as discussed below. It is not a strict classification, with some models presenting features of more than one group. Nonetheless, the GILA inversion is free from assumptions relative to any specific family, meaning that it is not in principle hindered from detecting these intermediate cases.

For each family, we select one or more representative interior models and apply the GILA inversion to their synthetic geodetic observables, assuming varying levels of gravity resolution and noise perturbation. The goal is to test the plausibility, in the frame of GILA and with realistic measurement settings, of both detecting the main features of a specific model and discerning models from different families. We mainly consider two extreme cases with regard to measurement settings (see Table 3):

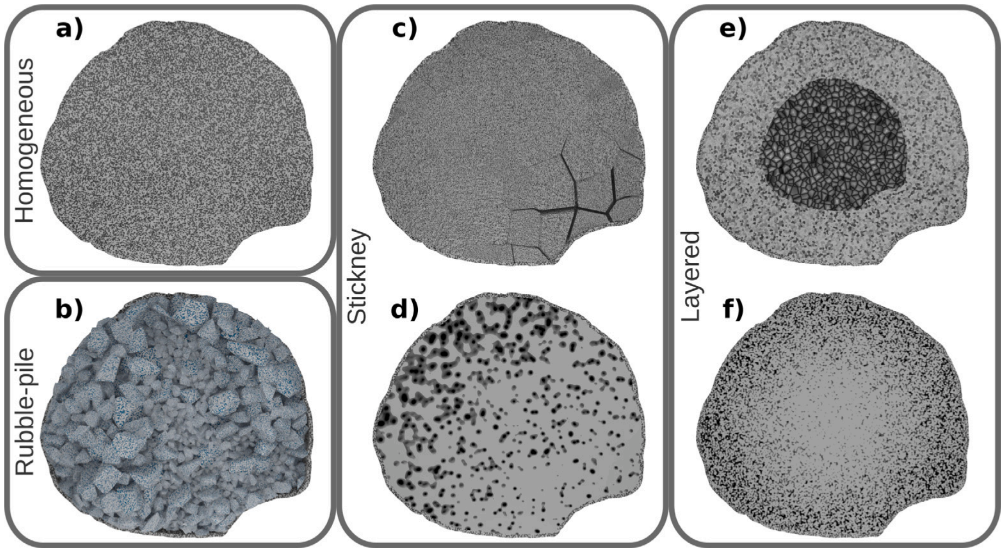

Fig. 2. Four families of interior for Phobos, based on models proposed in previous studies. Each picture is an artist's impression of a representative interior model, sliced along the equatorial plane of Phobos. The models include: a fully homogeneous body, at least at scales comparable to realistic resolutions of the observed gravity (a); a rubble-pile model (e.g. Le Maistre et al., 2019) with polydispersed blocks of ice-rock mixtures separated by voids (b); the Stickney models of Le Maistre et al. (2019), namely the Heavily Fractured (c) and the Porous Compressed (d); a layered model (Guo et al., 2021; Matsumoto et al., 2021; Dmitrovskii et al., 2022; Zhong et al., 2023; Yamamoto et al., 2024), with a lighter core (larger voids) homothetic to the external shape (e); a model with density increasing (porosity decreasing) towards the center, as considered by Dmitrovskii et al. (2022).

Table 3
Worst- and best-case noise settings for the synthetic tests.

Observable		Uncertainty	
		Pre-MMX	Post-MMX
Gravity	C_{20}	10%	0.1%
	C_{22}	30%	0.2%
	$\mathcal{O}_{lm}$	/	Eq. (2) ($l_{\max} = 4$)
Libration	θ	3%	1%
Obliquity	η	/	1%

- Pre-MMX: conservative settings, in preparation for real-data processing (Section 5); the measurements set replicates the data and uncertainties currently available: $10\,\%$ on C_{20}, $30\,\%$ on C_{22} (Yang et al., 2019) and $0.03°$ on the libration amplitude θ (accounting for the spread in its values of Table 1);
- Post-MMX: optimistic settings, based on best-case outputs of the MMX mission; the measurements set includes all $l_{\max} \leq 4$ gravity coefficients, with noise from Eq. (2), as well as libration and obliquity, with uncertainties of $0.01°$ and $0.04\,\mathrm{arcsec}$, respectively.

For each noise setting, we additionally evaluate the impact of the libration and obliquity measurements, by removing them from the dataset. For all the models examined and with the post-MMX settings, the impact of obliquity is minor when libration is also present, even with the very optimistic $1\,\%$ noise level (see Appendix B). Clearly, for more conservative uncertainties on the other observables, the effect of obliquity would be larger. Libration and obliquity have the same effect of constraining the principal moments of inertia, which is not possible from gravity alone (e.g. Le Maistre et al., 2019). Contrary to obliquity, libration has already been measured (Table 1), is one of the target measurements of MMX, and could realistically be observed at a lower relative uncertainty by the mission. We therefore only present the gravity and libration cases in the main text of this article.

4.1. Homogeneous

The homogeneous family includes models with spatially uniform distributions of porosity and ice/rock mixtures, assuming the size of the heterogeneities to be below the spatial resolution of the gravity field (Fig. 2a). The trivial case of a homogeneous moon can be easily verified by comparing the measured coefficients to those derived from the shape model. However, for the sake of providing an initial example of the GILA inversion, we show here a case where the ground-truth is a homogeneous distribution, which is used to generate noisy synthetic gravity coefficients with $l_{\max} = 4$.

As shown in Fig. 3, starting from a generic prior model (made up of a distribution of anomalies that is random in location and density), the size and density jumps of the anomalies are progressively reduced, until the model converges to a homogeneous distribution.[2] Nevertheless, especially given the presence of noise, a fully-homogeneous model is realistically not the only possible density distribution in agreement with the (homogeneous) synthetic measurements. Fig. 3a shows the cost function history for about 100 other runs. 35% of them converge earlier than the others (light green curves): they correspond to the fully-homogeneous solutions, where no mass anomaly remains at the end. The other solutions are forced by the system to reach 500 iterations. They present small (in size and density contrast) heterogeneities that have no statistical significance, which makes the final, averaged model consistent with a homogeneous density distribution, as shown in the bottom part of Figure 3.

Given the differences between the various Phobos shape models (Table 2), we tested the retrieval of a homogeneous distribution from synthetic observation generated via a different shape model. The resulting density solutions show a small degree of hetereogeneity, albeit of size smaller than the resolution of the $l_{\max} = 4$ gravity and thus not consistent in its spatial distribution across different solutions. Consequently, the estimated density contrasts over a range of density solutions are not statistically significant. Therefore, a homogeneous dataset would lead to a density solution with statistically insignificant heterogeneities, independently of the shape model used.

[2] Note that, in our approach, once an anomaly disappears it cannot be recreated simply though the least squares iterations, because the partials are only computed on the boundary of each anomaly: the homogeneous model is therefore a point of no return for our algorithm.

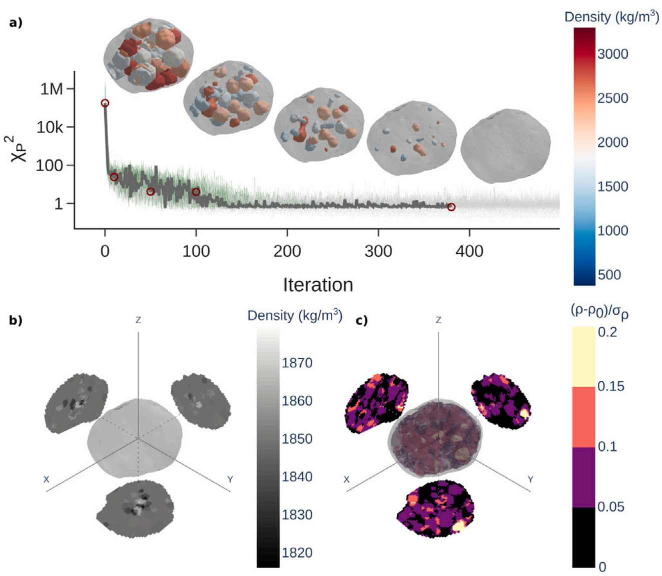

Fig. 3. Convergence history fitting noisy gravity data simulated for a homogeneous Phobos. The 3D plots represent the density solution at the iteration number indicated by the red circles, in the same order from left to right. The dark gray line shows the evolution of the cost function, represented by the reduced chi-squared statistic χ^2_P of the residuals, for the solution shown in the 3D plots. The cost function history for other 100 different runs over the same data (perturbed by random Gaussian noise) and starting from a random initial model, is also shown: in light green for those which converged to a fully homogeneous solutions (i.e. no remaining anomalies) and in light gray for those still exhibiting some level of heterogeneity after 500 iterations. Note that for the latter, the remaining mass anomalies are all small in size and have weak density contrasts with no statistical significance. Panels b and c show the average density distribution across all solutions, and the statistical significance of its density contrasts.

4.2. Rubble-pile

A rubble-pile structure for Phobos, involving solid irregular blocks separated by large voids, is consistent with its accretion from a debris disk, but could equally be the result of a captured asteroid having undergone catastrophic disruption (Asphaug et al., 1998).

As shown by Le Maistre et al. (2019), the expected values of the geodetic measurements associated to this family coincide with their homogeneous counterparts, owing to the randomness of the spatial distribution of voids. Le Maistre et al. (2019) considered, within the "Rubble Pile" family, a "Disrupted and Reaccreted" sub-family, where the random distribution of voids and rocks is fully contained beneath a 1 km-thick regolith layer: these particular models show instead clear heterogeneous signatures on the observables, due to the constant presence of the regolith layer. In this sense, the "Disrupted and Reaccreted" models could also be interpreted as 2-layer models, with the core approximating the average effects of all blocks dispersed within the internal region. The approximation of such a model by a 2-layer structure is even more apt when the size of the blocks is lower than the resolution of the gravity field, whose sensitivity to local density variations also decays with depth (e.g. Tricarico et al., 2021). The depth of the regolith layer on Phobos is poorly constrained, but expected to be below 100 m (Basilevsky et al., 2014), so whether its contribution to the gravity is significant enough is uncertain. We also include in this family models with ice-rock mixtures evenly dispersed within the body, as proposed by Dmitrovskii et al. (2022), because we expect the performance and limitations of our algorithm to apply in a similar way as with a (dry) rubble-pile. The "icy" models of Le Maistre et al. (2019), while also being formed by random distributions of ice and rock, are here classified as layered models, because the areas with ice/rock mixtures are confined to specific depths and, contrary to the "Disrupted and Reaccreted" subfamily, the size of the blocks of rock and ice is below realistic gravity resolutions.

Estimating of the size and density of the single components is obviously unrealistic, since the resolution of gravity is bound to be limited. Statistical characterization of bulk properties like porosity (e.g. Andert et al., 2010; Rosenblatt, 2011), ice/rock ratio (e.g. Pätzold et al., 2014; Kofman et al., 2015), and size-frequency distribution of the fragments (e.g. Tricarico et al., 2021) is routinely performed for small bodies. Here, instead, the focus is on the spatial distribution of the elements, which, if not uniform, might give rise to large-scale heterogeneities at a level detectable from gravity.

The interior of a rubble-pile Phobos is modeled via irregular fragments and voids, both with a polydisperse size-frequency distribution. Rocks and voids are here scattered in a matrix of uniform density, which accounts for the average effects of the smaller particles and voids. Fig. 4a shows an instance of such a rubble-pile structure, using a power-law size-frequency distribution as in Tricarico et al. (2021), with an exponent of −3. As the resolution of the gravity data only allows to image large-scale inhomogeneities, Fig. 4b shows the same interior model where the smaller elements have been removed for better visualization.[3] Fig. 4c shows the results of the simulated inversion using the pre-MMX noise settings, while results for the post-MMX noise model are shown in 4d. Multiple solutions have to be considered in order to identify artifacts and to explore the solution space. The corresponding average solution for 200 runs using the same measurement set (each time perturbed within its error bars) and a random initial model, is shown in the left column of each panel of Fig. 4. The top row of each panel represents gravity-only solutions, while solutions in the bottom row also fit the noisy synthetic libration measurement. For the post-MMX noise settings, the location of the main anomalous regions is correctly detected. These anomalies have a density contrast of the correct sign, although smaller in magnitude: the voids, in particular, are retrieved as $500\,\mathrm{kg/m^3}$ regions. However, such an error is within the standard deviation of the density values across all solutions, making these detected regions of negative density contrast consistent with voids. Moreover, as shown in the right column of Fig. 4d, the retrieved densities are statistically significant, having a mean contrast overall larger than their uncertainty (representing the spread of the density for each cell across all solutions). On the other hand, the pre-MMX solutions show little agreement with the ground-truth: unambiguous identification of the true model is not possible in this case, because both the number and accuracy of the data are too low, as is the signature of the target model on the measurements.

The inclusion of the libration observable does not substantially improve the detectability of the ground-truth model, even if, for the pre-MMX case, the detected heterogeneities have higher statistical significance, corresponding to a compression of the solution space. Still, some rubble-pile models may present a higher heterogeneous signature on libration, which is roughly normally distributed around the homogeneous value for this family (Le Maistre et al., 2019): for those models, the impact of the libration measurement would be larger.

4.3. Stickney

Constraints on the interior of Phobos could also come from its heavily cratered surface. The impact that caused the Stickney crater would have dispersed the moon had it been a monolith or a rubble-pile (Asphaug et al., 1998). In other words, the presence of the Stickney crater suggests that, at the time of that impact, Phobos was already porous, but stronger than a rubble-pile (Black and Mittal, 2015).

[3] Only anomalies larger than $\mathcal{V}\sin(\pi/l_{\max})/(2l_{\max})$ are kept, with $l_{\max} = 4$. This size corresponds roughly to the half-wavelength resolution of the spherical harmonics coefficients.

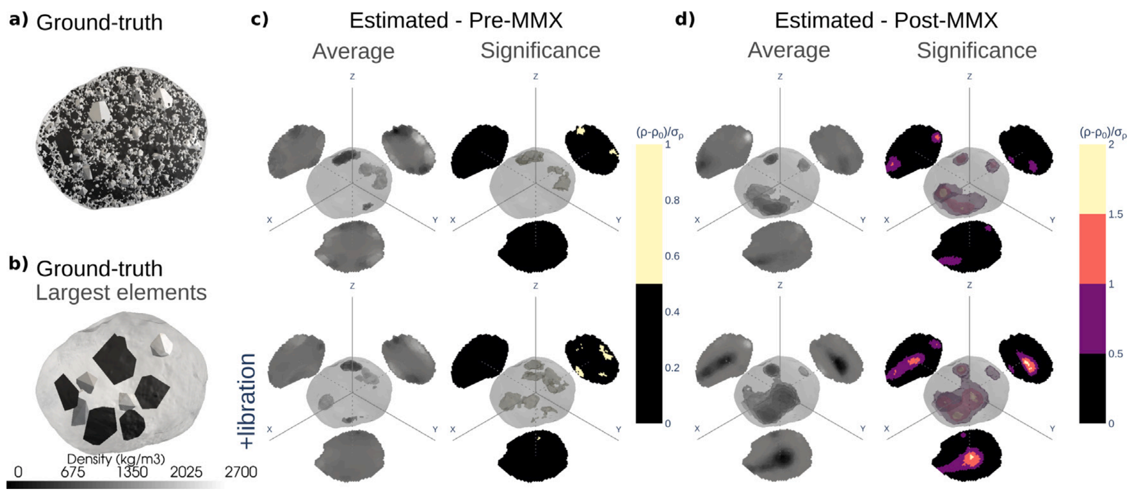

Fig. 4. Simulated retrievals for a rubble-pile ground-truth composed of voids and fragments of uniform density with a polydisperse size distribution: ground-truth model (a); largest blocks in the ground-truth model (b); average density solutions for the pre-MMX (c) and the post-MMX (d) noise settings. The pre-MMX settings replicate the uncertainty in the measured coefficients of Yang et al. (2019). In panels c and d: the top row is for gravity-only measurements, and the bottom row for gravity and libration; the left column shows the average solution and the right column its statistical significance.

Nonetheless, the Stickney impact probably generated additional damage within the body (Bruck Syal et al., 2016). The models in this class share a prominent anomaly below the Stickney crater. They include the Heavily Fractured (HF, Fig. 2c) and the Porous Compressed (PC, Fig. 2d) interiors of Le Maistre et al. (2019). These two families correspond to the effects of a Stickney-forming impact in the case of a porous body, where the energy is quickly absorbed via compression of material in a limited region below the crater, and of a coherent body, where instead the impact energy forms cracks which propagate through the body and leave a fractured structure below the crater (Asphaug et al., 1998). Models with a regional density anomaly below the Stickney crater have also been recently considered by Yamamoto et al. (2024) in the frame of MMX gravity estimation simulations. They showed how an anomaly below the crater could provide a detectable signal (higher than the expected noise) at $l_{max} = 4$.

We model both interior families by placing an ellipsoidal density anomaly under the crater, according to the numerical values in Table 2 of Le Maistre et al. (2019). The densities inside and outside the anomaly are also sampled within the range proposed therein. Fig. 5 shows the simulation results using the post-MMX settings, for different values of l_{max} in Eq. (2), up to the nominal $l_{max} = 4$. Of the models considered in Le Maistre et al. (2019), the Heavily Fractured and Porous Compressed are the ones showing the largest heterogeneous signature on the second-degree gravity (about 20% of the constant-density values), along with important signatures on C_{11} and S_{11}, which are here considered to be observable from orbit. It is for this reason that, already for $l_{max} = 2$ and without the inclusion of libration in the set of measurements, most of the solutions converge to distributions close to the ground-truth, with an anomalous mass below Stickney. What is shown here is the result of averaging similar solutions (as described in Section 3), thus generating a new solution, given the linearity of the density-only problem. Averaging leads to an anomalous mass that is closer to the ground-truth in terms of shape and symmetry compared to the single solutions, due to the removal of anomalies which are not statistically significant. Increasing the resolution of the gravity helps better refine the shape of the estimated anomaly and its statistical significance.

These models are also the ones showing the largest signature of the heterogeneities on the libration amplitude (Le Maistre et al., 2019), which is otherwise very small for other interior families, due to their distributions being on average radially symmetric. Anyway, even without the inclusion of the libration observable, the distributions of libration amplitudes associated to the gravity-only solutions of Fig. 5 are all roughly centered on the ground-truth value, itself about 10% away from the homogeneous value in both cases. Evidently, increasing the degree of gravity reduces the range of possible density solutions and thus the range of the moments of inertia and the resulting libration amplitudes. Indeed, the $l_{max} = 2$ case is the one impacted the most by the inclusion of libration, which increases the significance of the detected anomaly. Overall, however, the improvement on the retrieved models following the addition of the libration amplitude (and mean obliquity) measurement is marginal, given the already strong signal of these models in the gravity.

In Fig. 6, we present similar tests under the pre-MMX settings, which replicate the measurements uncertainty of Yang et al. (2019) observed coefficients. Compared to the $l_{max} = 2$ case above, where the noise level for degree-2 was 10% of the RMS of the degree-2 coefficients (meaning 5% on C_{20} and 10% on C_{22}), here the 1σ uncertainties are 10% for C_{20} and 30% for C_{22}. The larger uncertainty in the degree-2 gravity results in a wider distribution for the libration amplitudes of the gravity-only solutions. With these settings, the heterogeneous signal is fully below the noise level. Consequently, while the average gravity solutions do present an anomaly of the correct sign below the Stickney crater, that is only because the sets of randomly-sampled measurements have the ground-truth values as their central values. Accordingly, the detected anomalies have little statistical significance, and the solution is consistent with a homogeneous distribution. Adding the synthetic libration measurement does not introduce noticeable changes in the average solution. Notably, in this case the synthetic data also miss the degree-1, and thus the center of mass information. Therefore, compared to the $l_{max} = 2$ solutions of Fig. 5, the Stickney anomaly is accompanied here by other positive and negative anomalies around the equatorial plane, roughly separated by the half-wavelength of the C_{22} coefficient. For all these cases, the impact of the addition of the obliquity observable is also marginal (Appendix B).

4.4. Layered

Layered models have been proposed, based on geodetic measurements, by Guo et al. (2021) and Zhong et al. (2023). In particular, Guo et al. (2021) retrieved models with a lighter core in agreement with the gravity coefficients of Yang et al. (2019), assuming a shape of the core equal to that of Phobos[4] (see Fig. 2e) or equal to the best-fit ellipsoid

[4] As in Section 3.1.2, here simply referred to as *homothetic* core.

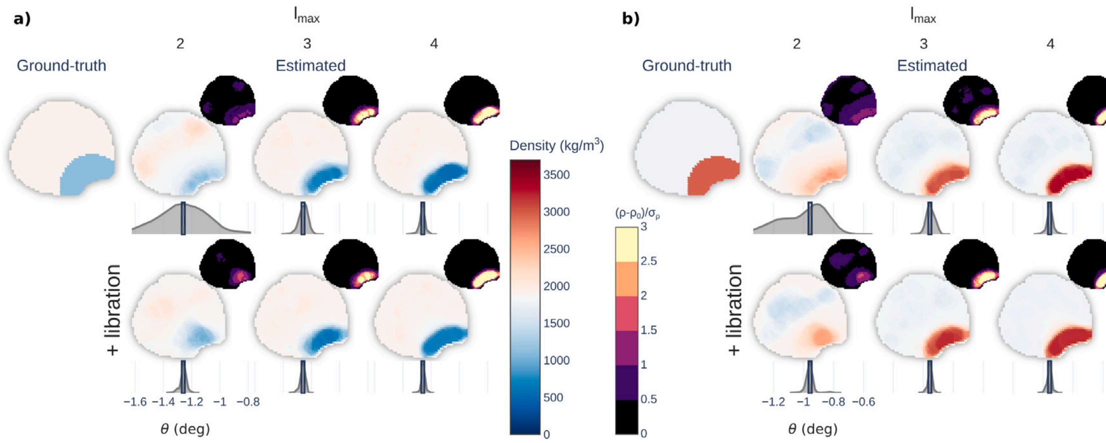

Fig. 5. Average density solutions for one model from the Heavily Fractured family (a) and one from model from the Porous Compressed family (b), for noise on the synthetic measurements given by Eq. (2) with varying l_{max} (columns). The larger 2D plots (diverging colorscale) are slices along the $z = 0$ plane ($+x$ towards the right and $+y$ towards the top) for average density solutions using gravity alone (top) and gravity with libration (bottom). The smaller 2D plots (discrete colorscale) show the statistical significance (as defined in Section 3) of the corresponding average density solution. The gray curve under each density plot shows the distribution of libration (θ) values across all solutions, with rectangles indicating the value associated to the ground truth and its assumed 1σ error of 0.01°, independently of its inclusion in the synthetic dataset.

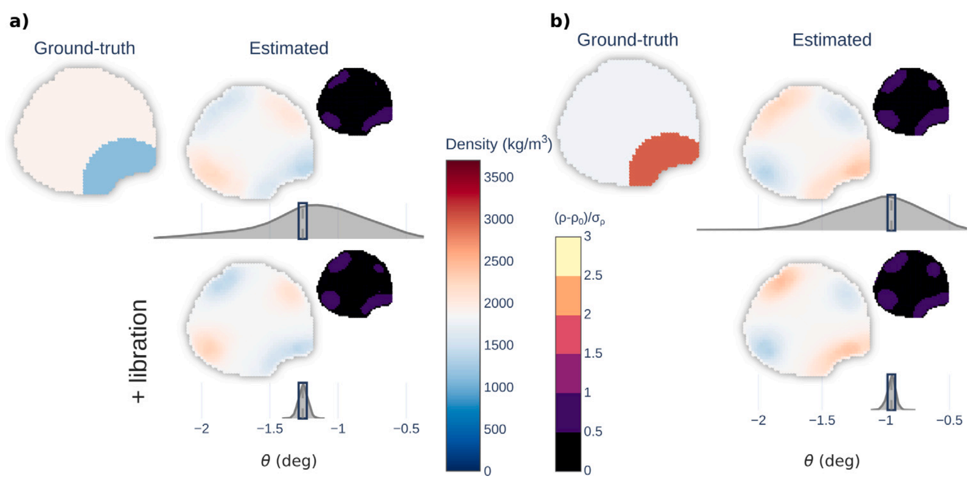

Fig. 6. Density solutions for one model from the Heavily Fractured family (a) and one model from the Porous Compressed family (b) with pre-MMX settings, hence assuming the gravity data uncertainty measured by Yang et al. (2019). Thus, C_{20} and C_{22} are the only gravity coefficients with signal higher than the noise. The noise level at 1σ is about 10% of the full value (but 150% of the heterogeneous signature) for C_{20} and 30% for C_{22} (about 5 times its deviation from homogeneous). The upper part in each panel represents gravity-only solutions, while the bottom part represents solutions using gravity and libration, the latter measurement affected by a 1σ error of 0.03° (Table 1). See Fig. 5 for a description of the plots.

representing Phobos' surface. Nonetheless, at least one layered model with a core denser than the mantle was also found, reflecting the high degeneracy of the density inversion from gravity, especially of such low resolution and high uncertainties. Similarly, Zhong et al. (2023) derived a model with a denser core from estimates of the mean moment of inertia (as computed from the degree-2 gravity and the libration amplitude). From a modeling perspective, a layered structure for Phobos has also been considered by Le Maistre et al. (2019) and Dmitrovskii et al. (2022). The "icy" families of Le Maistre et al. (2019) are based on the models of evolution of the water content of Phobos of Fanale and Salvail (1990): the "Icy Evenly Distributed" subfamily represents a Phobos initially containing ice all over its interior, while in the "Icy Surface Concentrated" the water ice was only present in a near-surface layer. For both models, insolation would have led to the ice escaping from the surface of Phobos, leaving a porous outer layer. Hence, the two subfamilies could be seen as 2-layer and 3-layer models, respectively. Le Maistre et al. (2019) show that the "Icy Evenly Distributed" models display large variability in their signature on the moments of inertia and the C_{20} and C_{22} coefficients, depending on the amount of water and voids assumed within the body, resulting however in libration amplitudes close to the homogeneous value. The "Icy Surface Concentrated" models behave similarly, albeit with a narrower range of variation in their signatures, given that the ice presence is limited to the middle layer.

Here we present the two extreme cases of a 2-layer model and one with a density gradient. The latter can be seen as the limit for an infinite number of layers. In Appendix C we show that it is realistically not feasible to distinguish between the two, even with optimistic precision and resolution of the geodetic measurements.

4.4.1. 2-layer models

Fig. 7 shows the expected performance of the GILA level-set inversion when the ground truth is a 2-layer model of Phobos, presenting as a single anomaly an homothetic core of varying size and density contrast. Specifically, the core density ranges from $500\,\mathrm{kg/m^3}$ to $3000\,\mathrm{kg/m^3}$, with the mantle density also varying in each case so as to have a bulk density of $1846\,\mathrm{kg/m^3}$. The different core sizes are instead obtained by scaling the outer shape of Phobos by a linear scale factor s_c, varying between

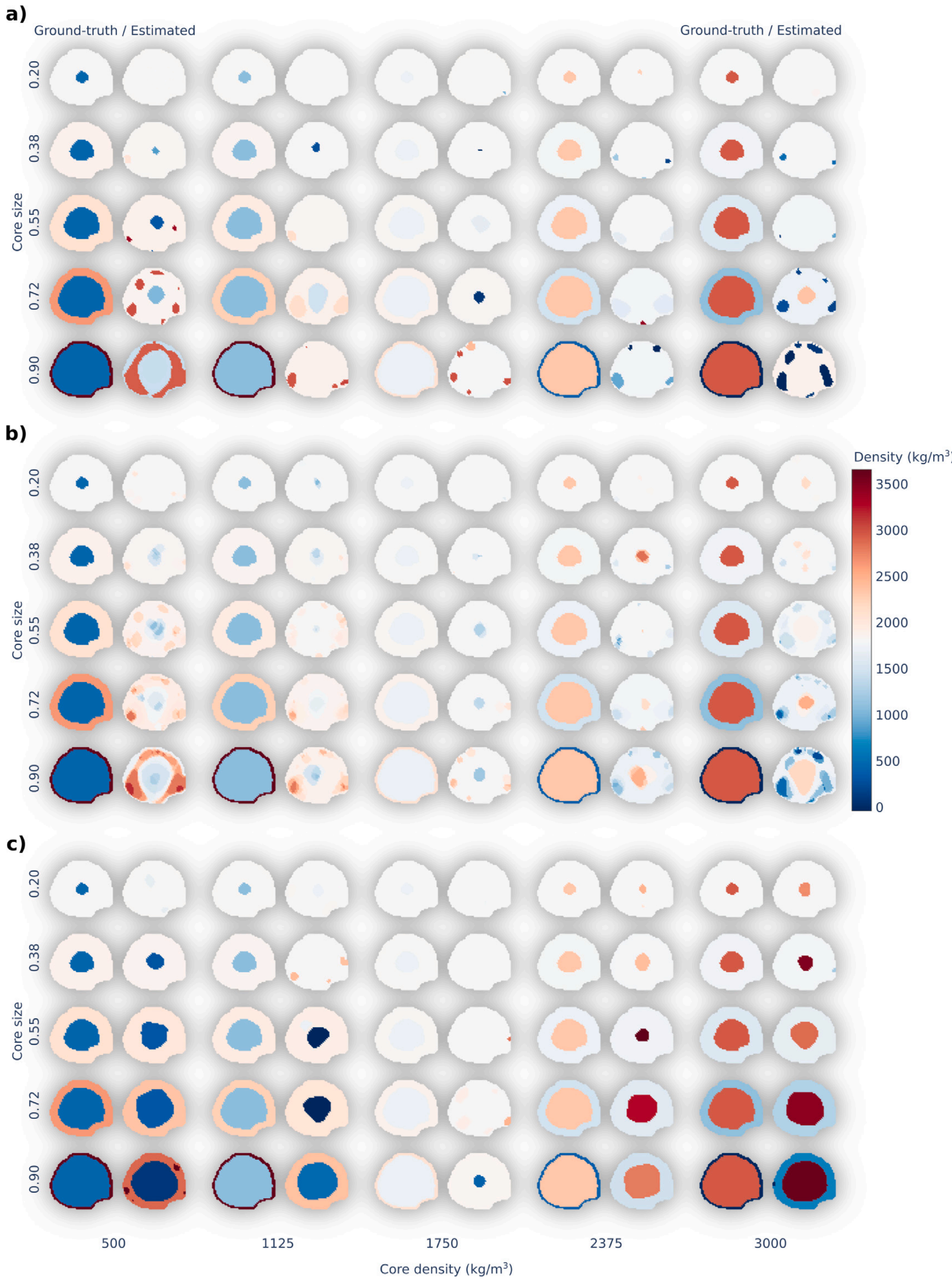

Fig. 7. Density solutions for 2-layer target models of different core densities (ρ_c from 500 to 3000 kg/m^3 along each row) and sizes (s_c from 0.2 to 0.9 along each column). Each pair of density plots, which are slices along the $z = 0$ plane of Phobos, shows the ground-truth (left) used to simulate noisy synthetic measurements and the corresponding solution (right). The panels represent single gravity-only solutions (a), average gravity-only solutions (b), and single solutions fitting gravity and libration. In all cases, the noise is given by the "post-MMX" settings of Table 3, with $l_{max} = 4$.

0.2 and 0.9. These ranges include all the possible core-size/density combinations found by Guo et al. (2021) and Zhong et al. (2023) to be compatible with the measured gravity coefficients, as well as the "Icy Evenly Distributed" family of Le Maistre et al. (2019).

In the first case, in Fig. 7a, the inversion is performed using gravity data alone. We show here only test cases based on the post-MMX noise settings (full degree-4 synthetic field as expected from MMX), but similar figures based on the pre-MMX settings can be found in Appendix D. Each pair of plots in the 5 × 5 matrix of core sizes and densities consists of slices along the $z = 0$ plane for the ground-truth model (on the left) and the density distribution estimated from the corresponding noisy synthetic geodetic observables (on the right). Most if not all of these solutions do not replicate the target distributions, although in many cases they do present a central anomaly of the correct sign, and larger in size the larger it is in the ground truth. This is to be expected given the degeneracy of a layered distribution for gravity.

In Fig. 7b, the rightmost distribution in each pair is obtained by averaging together multiple solutions (including those shown in Fig. 7a) converged from random initial distributions, and which fit data computed from the same ground-truth, but perturbed by random white noise. These average solutions display more clearly and consistently the presence of an inner core with a correct sign of the density jump. This is further proof that, as mentioned above, the central anomaly is correctly present in most of the models, and additional asymmetric features in the single solutions are the consequence of the limited resolution of the gravity. However, the density itself is generally different from that in the target distribution, given the different shape retrieved for the central anomaly.

The situation changes when libration is also added, as shown in Fig. 7c. Here the available data are sufficient to constrain the full tensor of inertia (within the measurement noise), making the 2-layer models no more a degenerate case.

4.4.2. Density gradient

As discussed in Caldiero and Le Maistre (2024), even if one of the main assumptions of the GILA level-set inversion is that the interior is composed of sharp density contrasts, in the case of smooth target distributions the converged, non-smooth solution might still represent a reasonable approximation of the true model. Furthermore, averaging enough solutions with sharp contrasts inevitably leads to distributions with smooth boundaries. Average solutions for the gradient-model ground-truth are shown in Figs. 8b for the pre-MMX noise settings and 8c for the post-MMX case. As in Fig. 4, the top row in each panel is relative to gravity-only solutions and the bottom row to gravity and libration solutions. The left column in each panel represents the average solutions and the right column their statistical significance, computed as the ratio of the average $\Delta\rho$ and its standard deviation over each element (Section 3).

As in the rubble-pile case, simulations based on the pre-MMX measurements uncertainties do not provide informative solutions, both with and without the inclusion of libration. They mostly comply with the lower value of C_{20} compared to the homogeneous (coming from the increase of the mass distribution towards the center of the body) by presenting a lower density at the equator and a higher density at the poles, as expected from Fig. 1. In addition to the smoothness of the ground-truth, however, the inversion here is also complicated by the degeneracy of the problem for this central distribution. Therefore, with the post-MMX settings ($l_{\max} = 4$), while correctly detecting a nearly-central, positive concentration of mass, even the average model cannot retrieve the rate of increase of the density with depth if no a priori information is provided to GILA. Injecting the libration information helps better define the nearly-symmetric distribution, but the average model still presents the characteristics of a 2-layer model. As shown in Appendix C, it is not realistically possible to distinguish a radial density gradient from a 2-layered distribution with the type and precision of the observables considered here.

5. Real data analysis

Here we apply the methods presented in the previous Sections to the interpretation of the gravity coefficients estimated by Yang et al. (2019), and the libration amplitude of Burmeister et al. (2018) and Lainey et al. (2021). As above, the shape model we use is that of Willner et al. (2014) because it is consistent with the gravity and libration solutions of these three studies.

5.1. Parametric estimation

Here, we target specific mass distributions inside Phobos: we apply Eqs. (8) and (9) to estimate 2-layer and radial-gradient models from the observed degree-2 gravity coefficients. This is done here via Markov chain Monte Carlo (MCMC) regression, by way of the PyMC Python library (Abril-Pla et al., 2023). For the 2-layer model, Eq. (8) is reparameterized for a more direct comparison with the results of Guo et al. (2021) and Zhong et al. (2023). The two free parameters are: the mantle density, $\rho_m = \rho_{CD} - \Delta\rho_c s_c^3$; the volume ratio of the core, $\lambda = s_c^3$. For the gradient model, the only free parameter is the density gradient, k, representing the difference between the density at the center of the body and that at the surface. The posterior distributions for the 2 models are shown in Fig. 9, assuming a multivariate normal distributions for the observables (C_{20} and C_{22}), with noise given by Yang et al. (2019) and no correlation. The priors on the parameters are chosen so as to favor densities in the range $[0, 3500]$ kg/m^3. In both cases, the posterior distributions tend to favor a lighter interior for Phobos, as found by Guo et al. (2021). However, given the large uncertainties associated with the data, the spread of the solutions also includes models with an interior denser than the surface. The solution proposed by Zhong et al. (2023) is not include in the range of 2-layer models though, possibly because it was meant to fit the mean moment of inertia, and not each gravity coefficient separately.

5.2. GILA inversion results

The GILA level-set inversion is then applied to the measured coefficients, sampled within their 1σ uncertainties (assuming no correlation) and starting from random initial density distributions, as done in the test cases of Section 4. No a priori assumption is made here on the density distribution inside Phobos. Then, as shown above, averaging the resulting converged solutions can help reduce overfitting and provide a density model of resolution closer to that of the gravity data. The final, averaged solution is characterized by a denser area around the equatorial region, and a lighter density at the poles. This is consistent with the higher (in magnitude) measured C_{20}, compared to the homogeneous value, and its interpretation given in Yang et al. (2019). The zonal degree-2 coefficient being the only measurement significantly different (at 3σ) from the homogeneous value and from 0, nothing meaningful can be inferred about the variation of the density with longitude when only gravity is considered. Overall, the shape of the average density distribution is reflected in the majority of the single solutions, suggesting an incomplete exploration of the solution space which is anyway unfeasible given the scarcity of the data and the non-linearity of the level-set approach. Moreover, a similar type of average density distribution was seen in most of the simulation tests performed with the Yang et al. (2019) noise profile in Section 4, save for the rubble-pile case, for which the signature on C_{20} was small. It is therefore not advisable to draw definitive conclusions about the interior of Phobos from these solutions alone.

Still, in order to better explore different trends in the set of obtained solutions, we now use k-means clustering to group together density distributions with similar characteristics (see details in Caldiero and Le Maistre (2024)). The gravity-only density solutions correspond to libration amplitudes roughly normally distributed around the homogeneous value of $\theta^{CD} = -1.14°$, with a mean of $-1.145°$ and a standard deviation of $0.2°$. As shown in Fig. 10a, clustering over the values of θ across all solutions, we obtain average solutions which maintain the general trend of a higher density at the equator and lighter density at the poles, but with higher concentration of the equatorial mass in the x direction for $|\theta| > |\theta^{CD}|$, and along the y axis for $|\theta| < |\theta^{CD}|$, as expected from the discussion on the signature of libration in Section 4.3.

The most recent measurements of libration (see Table 1) set this value close to θ^{CD} (Burmeister et al., 2018) or slightly lower in magnitude (Lainey et al., 2021). These two observables are alternately added

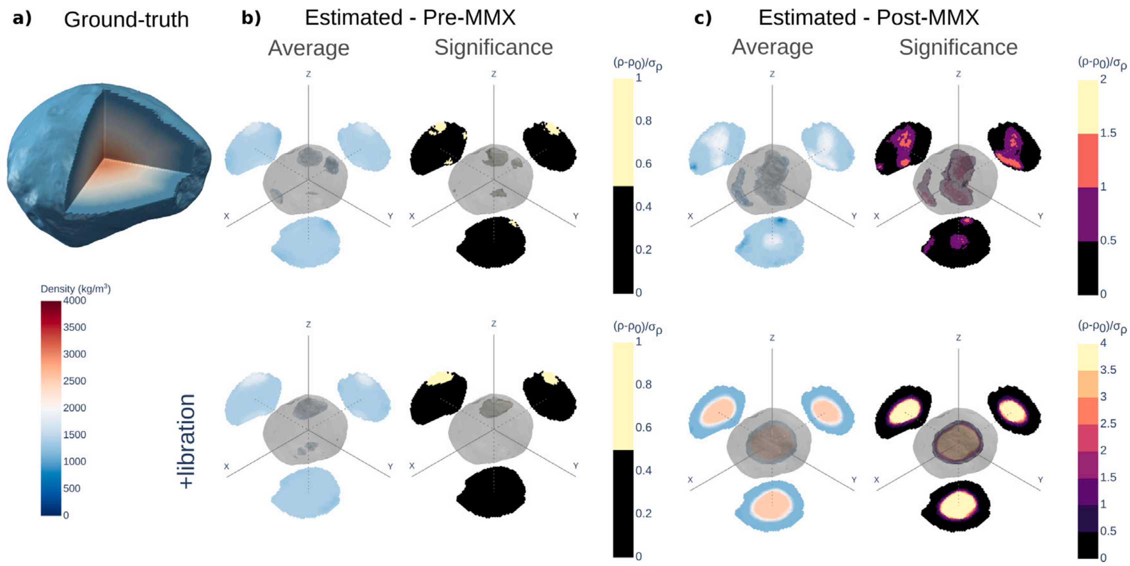

Fig. 8. Simulated retrievals for a target density distribution increasing linearly towards the center: ground-truth model (a); average solutions for the pre-MMX (l_{max} = 2, b) and the post-MMX (l_{max} = 4, c) noise settings (see Table 3). In panels b and c: the top row is for gravity-only measurements, and the bottom row for gravity and libration; the left column shows the average density solution (associated to the color-bar in the bottom left for the slices along the x=0, y=0, and z=0 planes, 3D mesh is not color-coded), and the right column shows its statistical significance with its own color-bar.

to the input dataset, using their measured uncertainties and assuming no correlation with the gravity. The corresponding average density solutions for the two cases are shown in the bottom panel of Fig. 10. As the Burmeister et al. (2018) libration is close to the homogeneous value, the resulting solution is similar to the $\theta \approx \theta^{CD}$ cluster of the gravity-only solution (central plot in Fig. 10a). The Lainey et al. (2021) libration leads to an average density solution which notably presents a positive mass anomaly in the vicinity of the Stickney crater, along with 3 others symmetrically distributed around the equator. In the majority of the single solutions, these symmetric equatorial anomalies appear in antipodal pairs, reflecting the ambiguity on the libration seen in Fig. 1a. This distribution is reminiscent of the results for the simulated Porous Compressed case of Fig. 6b, which was obtained assuming similar measurements settings, although in that case the 4 equatorial anomalies were alternating in sign. Realistically, the location of the anomaly in the real-data density solution is coincidental, due to Stickney being close to the line of 0 signature for libration (Fig. 1a). However, if indeed the actual interior of Phobos can be partly approximated by the Porous Compressed model, then, according to the results of Fig. 5, additional measurements (especially the degree-1 gravity coefficients) will be needed to remove the ambiguity in the location of the positive anomaly and effectively place a single anomaly under Stickney.

We however warn against over-interpretation of these results: both because of the assumptions in our methods and because of the non-linearity of the problem, they likely represent only a subset of possible density distributions in agreement with poorly accurate data. As an example, a libration amplitude close to homogeneous is consistent with layered or radial density distributions, as seen in Section 4.4. However, none of the solutions found here presents a layered structure, despite 2-layered models also being in agreement with the measured gravity, as seen above.

6. Discussion and conclusions

We have performed synthetic gravity inversion tests over plausible models for the interior of Phobos proposed in the past. The families of interior considered in this study include a fully homogeneous body, a loose rubble-pile structure with large voids separating monolithic blocks, a mass concentration or deficit under the Stickney crater, and layered or radial density distributions. Overall, the results presented above show how a degree-4 gravity field for Phobos, such as the one that might be measured by MMX, would dramatically improve our knowledge of its interior compared to the data currently available.

In order to narrow down the range of possible solutions in agreement with the data, we assume the target distribution to be composed of a limited number of zones where the density is uniform. The shape of these zones is modeled via the level-set formalism. The level-set functions and the density of each zone, and thus the interior density distribution, are estimated from a set of geodetic observables via iterative least-squares. We propose a range of plausible solutions in agreement with each dataset by repeating the inversion multiple times, starting from random initial density distributions and processing measurements perturbed within their given noise. The set of density solutions (eventually clustered into groups sharing common features) can be characterized in terms of its average density distribution and the statistical significance of eventual detected heterogeneities. The statistical significance is here intended, at each point inside the body, as the ratio of the density contrast in the average model and the spread of the density across all solutions of the set, the latter quantity representing the uncertainty on the estimated density. In this way, averaging multiple solutions allows to neglect heterogeneities smaller in size than the spatial resolution of the measurements and reduce overfitting. We refer the reader to Caldiero and Le Maistre (2024) for detailed explanation of the method, developed therein for gravity data only, and upgraded for the present study to process libration and obliquity data as well.

The simulation tests shown in Section 4, performed under realistic noise settings, show that for the post-MMX settings and for most of the models considered, the representative solution (average of multiple density solutions) is in good agreement with the ground-truth. When applied to synthetic data from a homogeneous ground-truth, the level-set algorithm converges to solutions with statistically insignificant heterogeneities, even when the shape-model used in the inversion is not the same as that of the ground-truth. In the single rubble-pile model considered here, the average density solutions correctly replicate the location of the largest voids and blocks in the interior, with statistically significant density contrast in agreement with those of the true models. Rocks and voids smaller than the resolution of the gravity do not appear in the average solution, as expected. The positive or negative anomaly in the Stickney models is equally well retrieved in the post-MMX synthetic tests. For all the cases mentioned above, the addition

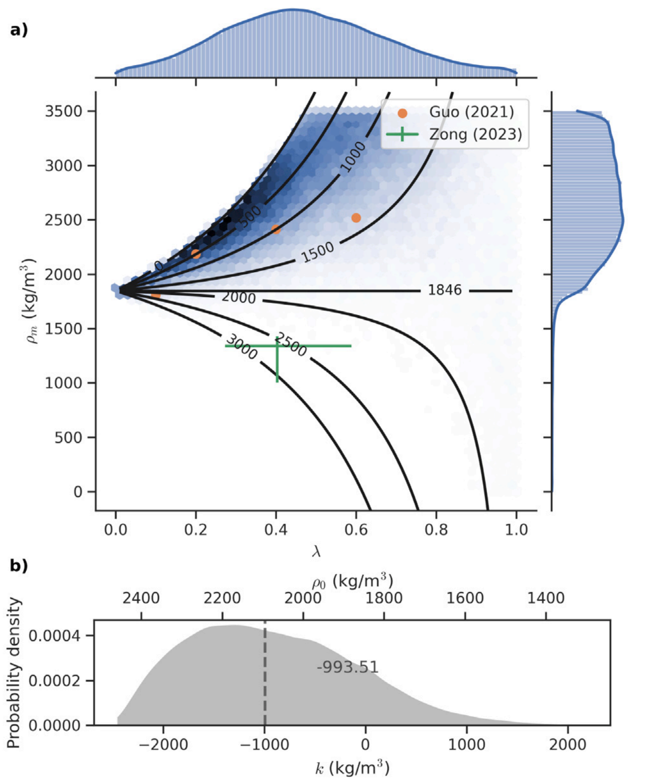

Fig. 9. MCMC fit of a core-mantle model (Eq. (8)) and a linear gradient model (Eq. (9)) to the (Yang et al., 2019) measured gravity coefficients. (a) 2-layer model: posterior distribution for the 2 free parameters, $\rho_m = \rho_{CD} - \Delta\rho_c s_c^3$ and $\lambda = s_c^3$, as a hexbin plot with marginal distributions at the sides; black contour lines represent the values of the core density $\rho_c = \rho_m + \Delta\rho_c$. The orange points are some of the 2-layers solutions found by Guo et al. (2021) from the same set of data, while the green error-bars show the range of the solutions estimated by Zhong et al. (2023) from the mean moment of inertia. (b) Linear gradient model: posterior plot for the single free parameter k; the dashed line indicates the median of the posterior distribution. Negative (positive) k corresponds to lighter (denser) core.

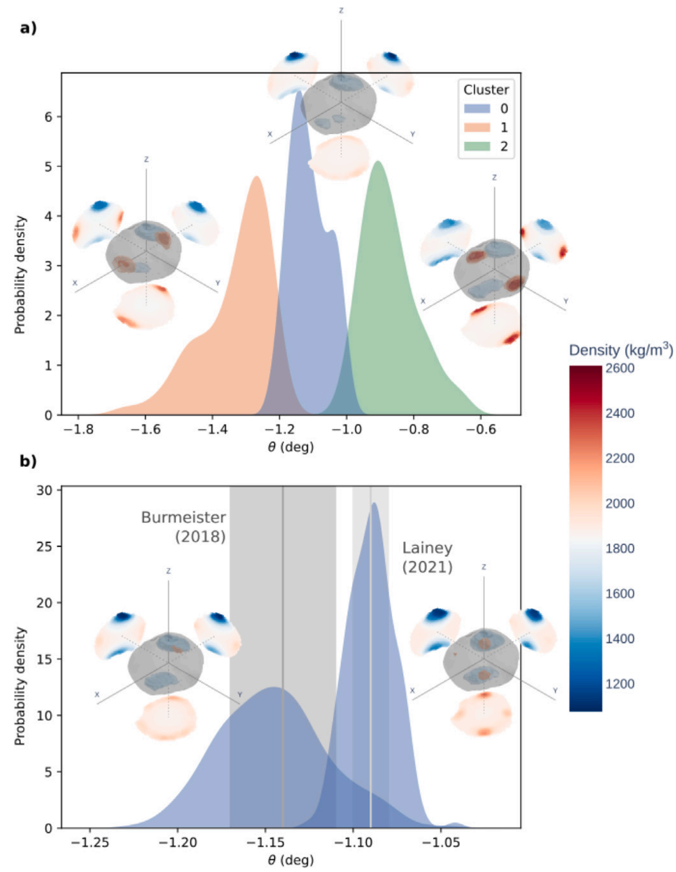

Fig. 10. Level-set inversion of the measured geodetic observables of Phobos. (a) average gravity-only density solutions from the Yang et al. (2019) observed coefficients; the solutions are grouped into 3 clusters based on their libration amplitude. (b) average density solution from Yang et al. (2019) gravity coefficients and the libration amplitudes measured by Burmeister et al. (2018) or by Lainey et al. (2021); vertical gray lines indicate the two measured libration values, and gray shaded areas their 1σ uncertainty bounds.

of the libration amplitude to the set of synthetic measurements does not influence substantially the average retrieved model, also because, as shown in Fig. 5, gravity degrees higher than 2 already constrain the libration values of the solutions to a narrow range around the true amplitude. On the other hand, the inclusion of the libration observable allows to additionally recover layered models, for which gravity could only provide the sign of the core density contrast. The inclusion of mean obliquity provides marginal improvements in the density solution, given the relatively low uncertainties on gravity and libration for the post-MMX settings.

The level-set inversion algorithm makes no assumption on the model to retrieve. However, a main limitation of our approach, also discussed in Caldiero and Le Maistre (2024), is its non-linearity, which precludes a complete exploration of the solution space, even when starting from a range of different initial conditions. For the pre-MMX cases, replicating the current uncertainty on the Phobos gravity field, the range of plausible solutions is realistically too large to be fully described by our algorithm. Even with a complete exploration of the solution space, pinpointing the ground-truth without additional information is unfeasible. For these reasons, we provide for some of these models expressions relating their signature on the geodetic observables to their characteristic parameters, which can then be estimated from the available data.

Applying the above methods to the measured Phobos degree-2 coefficients of Yang et al. (2019), we find that a linear decrease in density towards the center (a model introduced by Dmitrovskii et al., 2022) or a lighter core (as already demonstrated by Guo et al., 2021) can explain the gravity data. As for the level-set density solutions for these datasets, they predominantly present regions of higher density close to the surface in the equatorial plane and lower density at the poles, reflecting the signature of the measured C_{20} coefficient. Depending on the libration observable considered, the positive anomaly may extend over the whole equator (for the near-homogeneous θ measured by Burmeister et al. (2018)) or be concentrated in 4 symmetric regions close to the $y = \pm x$ direction (for the θ measured by Lainey et al. (2021)). Based on the current accuracy on the data, we can only go as far as to exclude the Heavily Fractured models, which present a lighter region under Stickney (as already suggested by Le Maistre et al. (2019)).

Comparing the synthetic "pre-MMX" $l_{\max} = 2$ cases (which often lead to average solutions similar to those obtained here with real data) with those of the "post-MMX" $l_{\max} = 4$ gravity, we see how the real-data case could reveal more about the true interior of Phobos following the observations of MMX. Even if tracking data from MMX 3D Quasi-Synchronous Orbits (QSOs) were not available, degree-1 coefficients, either measured by MMX or from astrometric observation, would resolve the ambiguity in the location of the positive equatorial anomalies detected here from the degree-2 data. Additionally, the improvements on our knowledge of C_{20} and C_{22} coming from MMX, even with planar QSOs alone (uncertainties down to a few percent), will narrow the range of solutions obtained in Section 5, and along with libration (and obliquity, if measurable) will further constrain the full tensor of inertia (Matsumoto et al., 2021).

CRediT authorship contribution statement

Alfonso Caldiero: Writing – original draft, Visualization, Software, Methodology, Investigation, Formal analysis. **Sébastien Le Maistre:** Writing – review & editing, Validation, Supervision, Project administration, Methodology, Investigation, Formal analysis, Conceptualization.

Declaration of competing interest

The authors declare that they have no known competing financial interests or personal relationships that could have appeared to influence the work reported in this paper.

Acknowledgments

The authors wish to thank Valéry Lainey and Amirhossein Bagheri for greatly improving the original manuscript with their comments, as well as Rose-Marie Baland and Antony Trinh for the discussion on Phobos rotation and interior. This work is funded by the French community of Belgium, within the frame of a FRIA, Belgium grant.

Appendix A. Signature on the observables

A.1. Point mass

If the anomaly is approximated by a single sphere of excess mass $\Delta\mathcal{M}$ (product of its density contrast and its volume) and radius R_S, fully contained within the body, we can derive expressions for its signature on the libration and the gravity harmonics. For the relative moment of inertia, appearing in the libration expression (Eq. (3)), we have:

$$\gamma = \frac{\gamma^{CD} C_0 + \Delta\mathcal{M}(x_S^2 - y_S^2)}{C_0 + \Delta\mathcal{M}\left(\frac{2}{5}R_S^2 + x_S^2 + y_S^2\right)} = \gamma^{CD} + \frac{\Delta\mathcal{M}\left[\frac{2}{5}\gamma^{CD}R_S^2 + x_S^2(1-\gamma^{CD}) - y_S^2(1+\gamma^{CD})\right]}{C_0 + \Delta\mathcal{M}\left(\frac{2}{5}R_S^2 + x_S^2 + y_S^2\right)}, \tag{11}$$

where (x_S, y_S, z_S) are the coordinates of the center of the anomaly and the 0 subscript refers to quantities for a homogeneous body of density equal to the background density ρ_0. Fig. 1a shows the relative signature on the libration ($\Delta\theta = \theta/\theta^{CD} - 1$) due to a point mass, as a function of its position over the $z = 0$ plane (Phobos equatorial plane) and the $y = 0$ plane. Here, the relative moment of inertia γ of the heterogeneous body is computed from Eq. (11) for the limit $R_S \to 0$, assuming a positive mass anomaly with $\Delta\mathcal{M}/\mathcal{M} = 0.1\,\%$. As the signature on γ is independent of the z position of the anomaly, the corresponding signature on libration is symmetric with respect to the $z = 0$ plane. The mass-anomaly being positive, Fig. 1a shows how a higher concentration of mass along the y-axis (higher I_{xx}) corresponds to a decrease in the magnitude of the libration amplitude, while concentrating the mass along the x-axis (higher I_{yy}) leads to an increase in magnitude for θ. This is true in general, and can be trivially justified based on Eq. (3), where an increase in γ corresponds to a relative decrease in θ, given that for Phobos $\gamma^{CD} \simeq 0.13 < 1/3$.

The contribution of the spherical anomaly to the gravity is the same as that of a point mass. Therefore, from Eq. (1) and as in Takahashi and Scheeres (2014), the spherical harmonic coefficients of a homogeneous body with one mass anomaly, $\Delta\mathcal{M}$, placed at (r_S, θ_S, ϕ_S) can be computed as:

$$\begin{bmatrix} C_{lm} \\ S_{lm} \end{bmatrix} = \left(1 - \frac{\Delta\mathcal{M}}{\mathcal{M}}\right)\begin{bmatrix} C_{lm}^{CD} \\ S_{lm}^{CD} \end{bmatrix} + \frac{\Delta\mathcal{M}}{\mathcal{M}}\frac{1}{(2l+1)}\left(\frac{r_S}{r_0}\right)^l \cdot P_{lm}(\cos\theta_S)\begin{bmatrix} \cos(m\phi_S) \\ \sin(m\phi_S) \end{bmatrix} \tag{12}$$

which for C_{20} and C_{22} simplifies to:

$$\begin{cases} C_{20} = \left(1 - \frac{\Delta\mathcal{M}}{\mathcal{M}}\right)C_{20}^{CD} + \frac{\Delta\mathcal{M}}{\mathcal{M}}\frac{\left(3z_S^2 - r_S^2\right)}{2\sqrt{5}r_0^2} \\ C_{22} = \left(1 - \frac{\Delta\mathcal{M}}{\mathcal{M}}\right)C_{22}^{CD} + \frac{\Delta\mathcal{M}}{\mathcal{M}}\frac{3\left(x_S^2 - y_S^2\right)}{2\sqrt{15}r_0^2}, \end{cases} \tag{13}$$

where x_S, y_S, z_S are the cartesian coordinates of the sphere's center. As done for the libration amplitude, the signature of a positive point-mass on C_{20} and C_{22} is shown in Fig. 1. The spatial distribution of the signature of a point-mass on C_{22} is highly correlated with that of the signature of a point mass on libration. The conclusions drawn for the libration plot therefore also apply to C_{22}. Libration and C_{22} carry similar spatial information, meaning, as shown below, that the impact of the inclusion of the libration observable is reduced when C_{22} is far from homogeneous and well-constrained.

A.2. Spherical layers

We give here formulas for the gravity and libration amplitude of layered models with spherical layers, all centered on Phobos' center-of-figure.

For N spherical layers, the relative moment of inertia is given by:

$$\gamma = \frac{\mathcal{B}_0 - \mathcal{A}_0}{C_0 + \frac{8}{15}\pi\sum_{i=1}^N \Delta\rho_i R_i^5} = \frac{C_{CD}}{C_{CD} + \frac{8}{15}\pi\frac{\rho_{CD}}{\rho_0}\sum_{i=1}^N \Delta\rho_i R_i^5}\gamma^{CD}. \tag{14}$$

We remind that the specifications CD and 0 refer to properties of a constant-density Phobos with density equal to the bulk density (ρ_{CD}) and the background density (ρ_0), respectively. The deviation of the gravity coefficients from their homogeneous values ($\mathcal{O}_{lm}^{CD}$) is

$$\Delta\mathcal{O}_{lm} = \mathcal{O}_{lm} - \mathcal{O}_{lm}^{CD} = -\frac{4}{3}\pi\frac{\sum_{i=1}^N \Delta\rho_i R_i^3}{\mathcal{M}}\mathcal{O}_{lm}^{CD} \tag{15}$$

where the total mass is given by

$$\mathcal{M} = \rho_0\mathcal{V} + \frac{4}{3}\pi\sum_{i=1}^N \Delta\rho_i R_i^3 = \rho_{CD}\mathcal{V} \tag{16}$$

For a single core, Eq. (15) is equivalent to Eq. 20 in Takahashi and Scheeres (2014). In that case, as understood from Eqs. (14), (15), and (16) above, libration and gravity data are sufficient to determine the radius and density contrast of the core. On the other hand, gravity and libration alone do not allow to uniquely determine a layered structure in the core, as any distribution with spherical layers gives the same observable as a 2-layer model with core size:

$$R_c = \sqrt{\frac{\sum_{i=1}^N \Delta\rho_i R_i^5}{\sum_{i=1}^N \Delta\rho_i R_i^3}}. \tag{17}$$

A.3. Homothetic layers

For an interior with N homothetic layers, thus with the same shape as Phobos, but scaled by a factor s_i (ratio between the maximum radius of the layer and that of the external shape), we have:

$$\gamma = \gamma^{CD} \tag{18}$$

since the moments of inertia of each anomaly are proportional to those of the uniform body, with the same factor of $s_i^5\Delta\rho_i/\rho_{CD}$ applying to all 3 principal moments of inertia. The gravity coefficients of each layer are instead given by $s_i^l \mathcal{O}^{CD}_{lm}$, since everything in Eq. (1) is scaled-down, save for the reference radius r_0. Hence, the heterogeneous signature of N layers on a coefficient of degree l and order m is:

$$\Delta\mathcal{O}_{lm} = \frac{\sum_{i=1}^{N} \Delta\rho_i s_i^3 (s_i^l - 1)}{\rho_{CD}} \mathcal{O}^{CD}_{lm}, \tag{19}$$

with the mass equal to:

$$\mathcal{M} = \left(\rho_0 + \sum_{i=1}^{N} \Delta\rho_i s_c^3\right) \mathcal{V} = \rho_{CD}\mathcal{V} \tag{20}$$

For a single homothetic core of scale factor s_c and density contrast $\Delta\rho_c$, Eq. (19) becomes Eq. (8) in the main text.

In this 2-layer case, as the equations for coefficients of different degrees are independent, $\Delta\rho_c$ and s_c can be determined already from degree-2 gravity, assuming infinitely accurate and precise measurements, as:

$$\begin{cases} \Delta\rho_c = \frac{\Delta C_{10}\rho_{CD}}{C_{10}^{CD} s_c^3 (s_c - 1)}, \\ s_c = \frac{\Delta C_{20}}{\Delta C_{10}} \frac{C_{10}^{CD}}{C_{20}^{CD}} - 1. \end{cases} \tag{21}$$

If the system were linear, in order to detect N homothetic boundaries and the corresponding density contrasts, we would need $2N$ independent equations, which would come from a set of measured gravity coefficients of maximum degree $2N$. This is a lower boundary, since the terms in s^l may admit multiple positive roots. However, since in the level-set inversion we do not make the *a priori* assumption of a homothetic core, we do not expect good retrievals from gravity data alone. The libration information helps reduce the range of possible models to those for which γ is the same as the homogeneous value, and thus should lead the method to more easily converge to layered models.

A.4. Density gradient

We additionally consider here models with a radial density gradient (Fig. 2f), as presented in Dmitrovskii et al. (2022), corresponding to the ground-truth model shown in Fig. 8a. To a first approximation, this model can be seen as a homothetic layered model for the limit of the number of layers $N \to \infty$. The corresponding gravity observables can be obtained by transforming the sum in Eq. (19) into an integral:

$$\Delta\mathcal{O}_{lm} = -\frac{\mathcal{O}^{CD}_{lm}}{\rho_{CD}} \int \frac{d\rho(s)}{ds} s^3 (s^l - 1) ds \tag{22}$$

where the negative sign is introduced because $\Delta\rho_i$ in Eq. (19) is computed as the difference between the density of the inner layer and that of the outer layer, hence in the opposite direction of the positive incremental core-size, ds. Assuming a density varying linearly with the depth, i.e. $\rho(s) = \rho_0 + k(1 - s)$, and s in the range $[0, 1]$, meaning the density varies from ρ_0 at the surface to $\rho_0 + k$ at the center, we obtain Eq. (9) in the main text. The parameters k and ρ_0 can already be determined from a single (perfectly known) gravity coefficient of any degree, and from the mass balance:

$$\mathcal{M} = \left(\rho_0 + \frac{k}{4}\right) \mathcal{V} = \rho_{CD}\mathcal{V} \tag{23}$$

However, as in general $\mathcal{O}^{CD}_{lm}/\rho_{CD} \ll 1$, the uncertainties in the single coefficients are largely amplified when estimating k, so that multiple observations are needed.

More generally, for a linear density variation between 2 depths, s_0 and $s_1 > s_0$:

$$\Delta\mathcal{O}_{lm} = -\frac{\mathcal{O}^{CD}_{lm}}{\rho_{CD}} \frac{k}{4} \left[s_1^4 - s_0^4 + \frac{4\left(s_0^{4+l} - s_1^{4+l}\right)}{4+l} \right], \tag{24}$$

and the total mass is given by:

$$\mathcal{M} = \left[\rho_0 \left(s_1^3 - s_0^3\right) + k\left(s_1^3 \left(1 - \frac{3s_1}{4}\right) - s_0^3 \left(1 - \frac{3s_0}{4}\right)\right)\right] \mathcal{V}. \tag{25}$$

Such a model could therefore represent a smooth transition between two layers of different density.

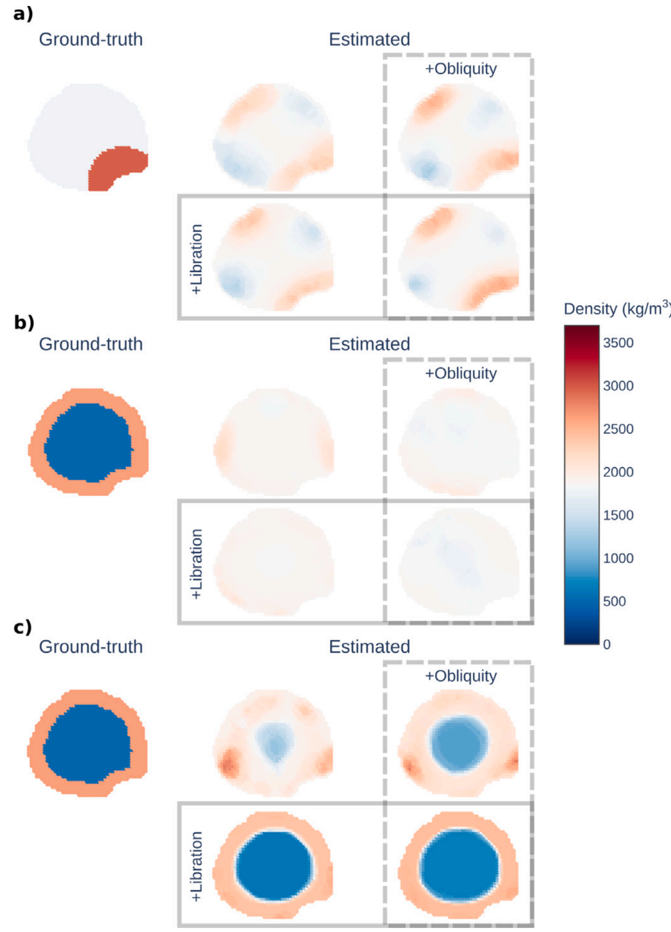

Fig. 11. Impact of the obliquity observable on GILA simulations. Each panel shows the averaged solutions fitting synthetic measurements of different ground truth (Porous Compressed in panel a, 2-layered in panels b and c) and noise settings (pre-MMX in panels a and b, post-MMX in panel c). Within each panel, next to the ground truth, the four quadrants show estimated density maps inferred from gravity only (top left), gravity and libration (bottom left), gravity and obliquity (top right) and gravity, libration and obliquity (bottom right).

Appendix B. Contribution of obliquity data

The linearized expression for the obliquity (Eq. (5)) allowed us to easily implement the partial derivatives in GILA. The results show little improvement to the accuracy of the retrievals when obliquity is added to the synthetic observables. Fig. 11 shows simulated density estimations for some of the models and noise settings considered in the manuscript, where libration, obliquity (at the very optimistic 1% noise level), or both, are alternately added to the synthetic gravity measurements. In our approach obliquity and libration have the same effect of complementing the degree-2 gravity for the determination of the moments of inertia. For the pre-MMX settings, the uncertainty on the moments of inertia is limited by the 30% uncertainty on C_{22}: in that case, even a 10% uncertainty on the obliquity is enough to reduce the error on the moments of inertia to about 10%, which is a lower limit due to the 10% uncertainty on C_{20}. In the post-MMX noise settings, gravity and libration are already sufficient to constrain the principal moments of inertia at the percent level. Unless uncertainties on the obliquity much lower than those on libration are assumed, which would be unrealistic, the resulting uncertainty on the moments of inertia does not change substantially with the inclusion of obliquity. This could explain its very small contribution to the retrieved density maps, as shown in Fig. 11c.

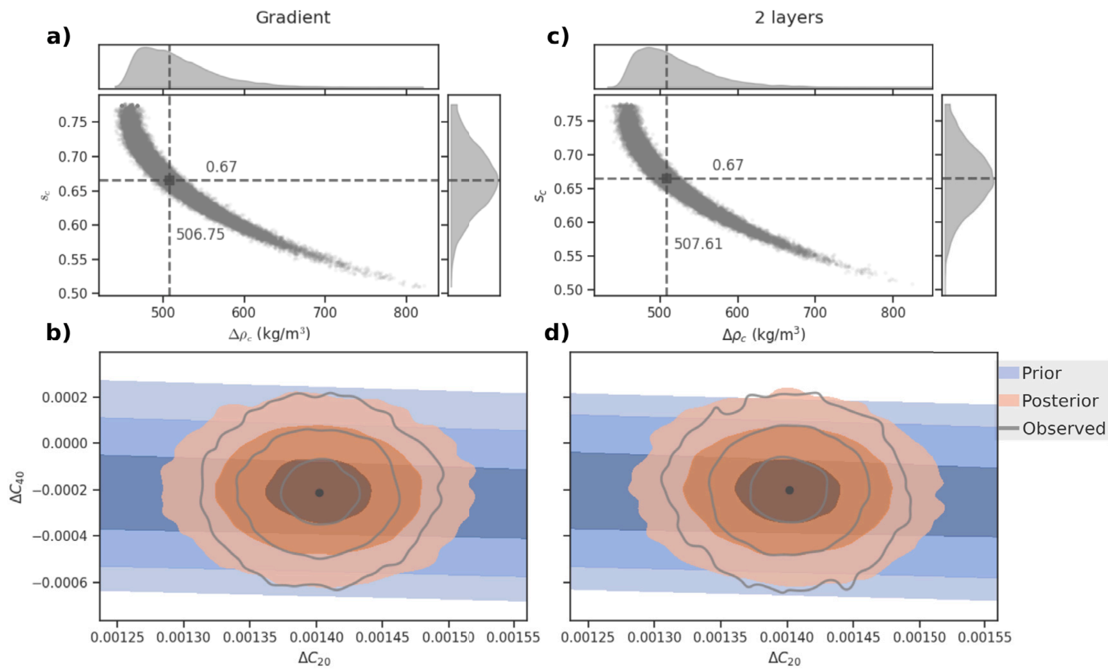

Fig. 12. MCMC inference of the parameters $\Delta\rho_c$ and s_c of a 2-layer model (Eq. (8)) from noise-free data generated from: the linear gradient model (Eq. (9)) with $k = 1000\,\mathrm{kg/m^3}$ (a); the same 2-layer model (Eq. (8)) with $\Delta\rho_c = 506.25\,\mathrm{kg/m^3}$ and $s_c = 2/3$ (c). Dashed lines mark the median values of the marginal posterior distributions. Predictive checks for the two cases are shown in panels b and d, respectively: concentric shapes delimit the 1,2, and 3σ bounds for the C_{20} and C_{40} values predicted from the prior (blue areas) and from the posterior (orange areas), or sampled from a multivariate normal distribution with the observed mean and covariance (gray lines).

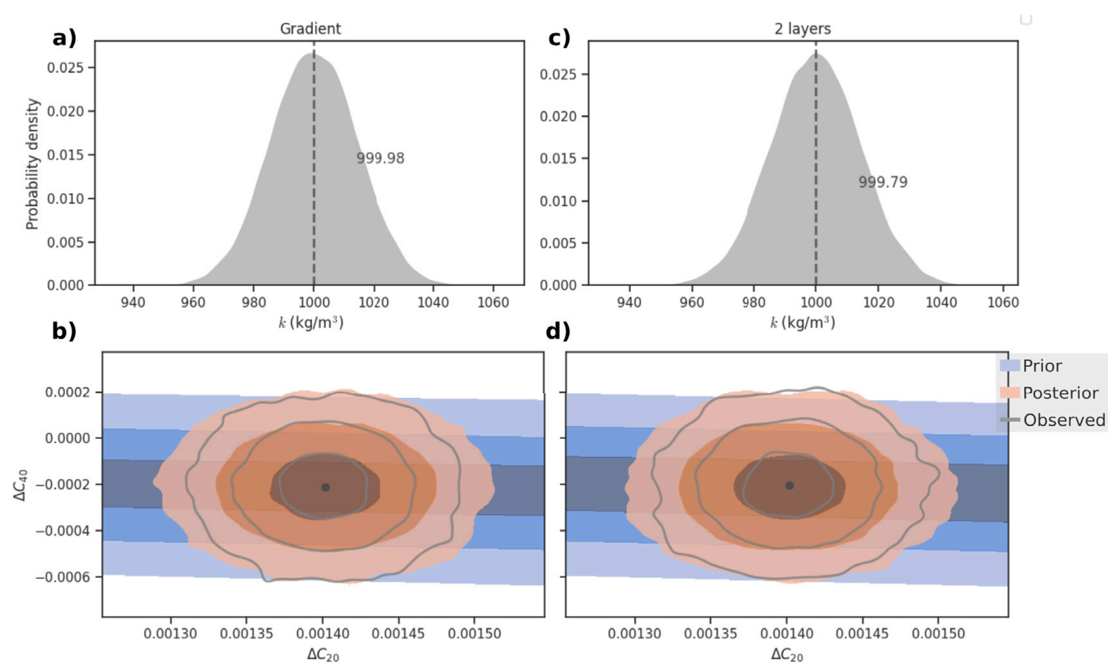

Fig. 13. MCMC inference of the parameter k of a linear-gradient model (Eq. (9)) from noise-free data generated from: the same linear gradient model (Eq. (9)) with $k = 1000\,\mathrm{kg/m^3}$ (a); the 2-layer model (Eq. (8)) with $\Delta\rho_c = 506.25\,\mathrm{kg/m^3}$ and $s_c = 2/3$ (c). Dashed lines mark the median values of the posterior distributions. Predictive checks for the two cases are shown in panels b and d, respectively: concentric shapes delimit the $1-$, $2-$, and 3σ bounds for the C_{20} and C_{40} values predicted from the prior (blue areas) and from the posterior (orange areas), or sampled from a multivariate normal distribution with the observed mean and covariance (gray lines).

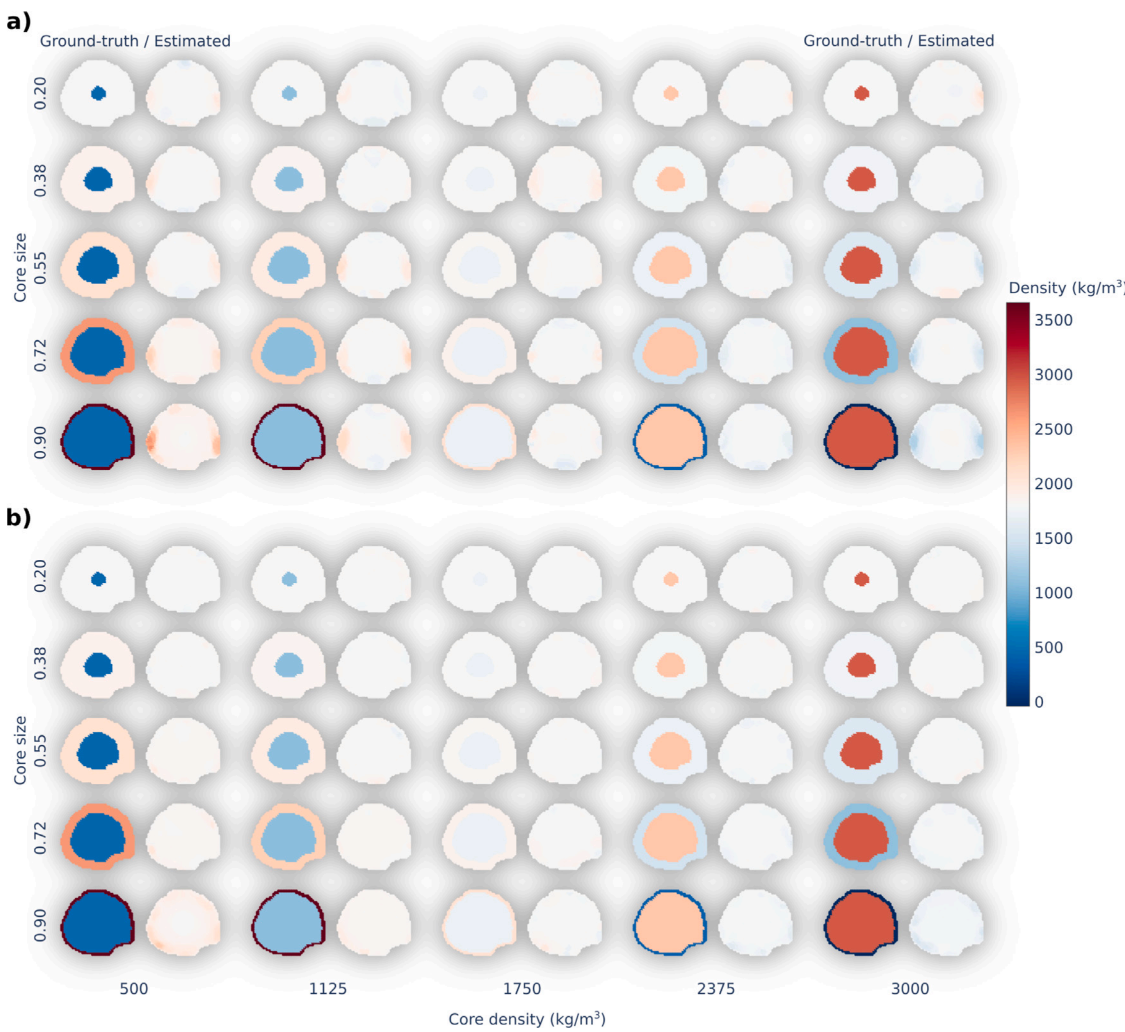

Fig. 14. Simulated density solutions for 2-layer target models of different core densities (ρ_c from 500 to 3000 $\mathrm{kg/m^3}$ along each row) and sizes (s_c from 0.2 to 0.9 along each column). Each pair of density plots, which are slices along the $z = 0$ plane of Phobos, shows the ground-truth (left) used to simulate noisy synthetic measurements and the corresponding solution (right). The panels represent average gravity-only solutions (a), and average solutions fitting gravity and libration. The measurement noise replicates the Yang et al. (2019) observed uncertainties for the mass and the gravity coefficients (only C_{20} and C_{22} are statistically significant) and is 0.03° for libration (Table 1).

Appendix C. Density gradient versus layered model

By comparing the expressions for the gravity and mass of the 2-layer model and of the density gradient model, we see that the system of equations relating the two is in general not consistent. Still, given the uncertainty on the measurements, it is possible to find a least-squares solution for the parameters $\Delta\rho_c$ and s_c of the single core model that agree with the observables coming from a gradient model with given ρ_0 and k. Therefore, even with libration (close to θ^{CD}) constraining the models to be layered or with a linear gradient, most of the solutions and the final averaged model (Fig. 8c, bottom panel) share a simple 2-layer configuration.

As an example of the proximity of the two models, we consider a positive-gradient model with $k = 1000\,\mathrm{kg/m^3}$ and $\rho_0 = 1596\,\mathrm{kg/m^3}$, which has the nominal bulk density of $\rho_{CD} = 1846\,\mathrm{kg/m^3}$ (Eq. (23)). The parameters for a compatible 2-layer model can be retrieved according to Eq. (21), using $\Delta C_{10}/C_{10}$ and $\Delta C_{20}/C_{20}$ computed via the gradient-model equations (Eq. (9)), giving $\Delta\rho_c = 506.25\,\mathrm{kg/m^3}$, $s_c = 2/3$. With the 2-layer model parameters thus computed, the median relative error between the sets of coefficients corresponding to the compatible 2-layer and gradient models is, up to degree 4, about 7%, with the relative difference between the heterogeneous signatures (right-hand sides of Eqs. (21) and (9)) only reaching 20% for degree-12 coefficients. This corresponds to a difference of less than 1% relative to the full homogeneous values, meaning that a gravity field of $l_{\max} \geq 8$ would be needed for this signal to be above the measurements noise (assumed to follow Eq. (2) with $\alpha = 0.1$) for most of the coefficients.

In a realistic scenario, with measurements affected by errors, Eq. (21) (using only 2 measurements to determine the parameters of a 2-layer model) should be replaced by a more proper regression over all available coefficients. This is done here via Markov chain Monte Carlo (MCMC) regression over the parameters of the 2-layer model (Eq. (8)), by way of the PyMC Python library (Abril-Pla et al., 2023). As shown in Fig. 12, using as observables noise-free, $l_{max} = 4$ gravity coefficients computed for a gradient model with $k = 1000\,\mathrm{kg/m^3}$, we obtain posterior distributions for s_c and $\Delta\rho_c$ of a 2-layer model which are consistent with the values computed above via Eq. (21).

In Fig. 13, we show MCMC simulations for the opposite case, that of estimating a density gradient from noise-free, $l_{max} = 4$ data corresponding to the 2-layer model defined above. The posterior distribution for the parameter k is centered around a value close to $1000\,\mathrm{kg/m^3}$, corresponding to the parameter of the compatible gradient model as defined above, and leads to predicted observables in good agreement with the data. It is therefore unlikely for the level-set method to converge to a smooth density-gradient distribution in a realistic case. On the other hand, data with heterogeneous signatures varying by degree and constant across each degree might indicate the presence of a layered (homothetic) structure, and the simple expression for the gravity signatures in Eq. (9) can be used to estimate the parameters of a gradient model.

Appendix D. 2-layers simulations with current data uncertainties

Fig. 14 shows, similarly to Fig. 7, the average GILA solutions for ground-truths composed of a single core of varying size and density contrasts. Here the uncertainties are those of Yang et al. (2019), meaning ∼10% on C_{20} and ∼30% on C_{22}. Compared to the $l_{\max} = 4$ plots in Fig. 7, here the density contrasts in the solutions are much fainter, even with the inclusion of libration in the dataset: given the large uncertainty in the data, most of the solutions are consistent with a homogeneous distribution.

Data availability

The code for GILA, which was used to generate the data presented in this paper, is available on GitLab https://gitlab-as.oma.be/sbm/gila.

References

Abril-Pla, O., Andreani, V., Carroll, C., Dong, L., Fonnesbeck, C.J., Kochurov, M., Kumar, R., Lao, J., Luhmann, C.C., Martin, O.A., Osthege, M., Vieira, R., Wiecki, T., Zinkov, R., 2023. PyMC: A modern, and comprehensive probabilistic programming framework in Python. PeerJ Comput. Sci. 9, e1516. http://dx.doi.org/10.7717/peerj-cs.1516.

Andert, T.P., Rosenblatt, P., Pätzold, M., Häusler, B., Dehant, V., Tyler, G.L., Marty, J.C., 2010. Precise mass determination and the nature of Phobos. Geophys. Res. Lett. 37 (9), http://dx.doi.org/10.1029/2009GL041829.

Asphaug, E., Ostro, S.J., Hudson, R.S., Scheeres, D.J., Benz, W., 1998. Disruption of kilometre-sized asteroids by energetic collisions. Nature 393 (6684), 437–440. http://dx.doi.org/10.1038/30911.

Bagheri, A., Khan, A., Efroimsky, M., Kruglyakov, M., Giardini, D., 2021. Dynamical evidence for Phobos and Deimos as remnants of a disrupted common progenitor. Nat. Astron. 5 (6), 539–543. http://dx.doi.org/10.1038/s41550-021-01306-2.

Baland, R.M., Hoolst, T.V., Yseboodt, M., Karatekin, Ö., 2011. Titan's obliquity as evidence of a subsurface ocean? Astron. Astrophys. 530, A141. http://dx.doi.org/10.1051/0004-6361/201116578.

Basilevsky, A.T., Lorenz, C.A., Shingareva, T.V., Head, J.W., Ramsley, K.R., Zubarev, A.E., 2014. The surface geology and geomorphology of Phobos. Phobos, Planet. Space Sci. Phobos, 102, 95–118.http://dx.doi.org/10.1016/j.pss.2014.04.013,

Black, B.A., Mittal, T., 2015. The demise of Phobos and development of a Martian ring system. Nat. Geosci. 8 (12), 913–917. http://dx.doi.org/10.1038/ngeo2583.

Bruck Syal, M., Rovny, J., Owen, J.M., Miller, P.L., 2016. Excavating Stickney crater at Phobos. Geophys. Res. Lett. 43 (20), 10,595–10,601. http://dx.doi.org/10.1002/2016GL070749.

Burmeister, S., Willner, K., Schmidt, V., Oberst, J., 2018. Determination of Phobos' rotational parameters by an inertial frame bundle block adjustment. J. Geod. 92 (9), 963–973. http://dx.doi.org/10.1007/s00190-018-1112-8.

Burns, J.A., 1992. Contradictory clues as to the origin of the martian moons. In: Kieffer, H.H., Jakosky, B.M., Snyder, C.W., Matthews, M.S. (Eds.), Mars. University of Arizona Press, pp. 1283–1302. http://dx.doi.org/10.2307/j.ctt207g59v.42.

Caldiero, A., Le Maistre, S., 2024. Small bodies global gravity inversion via the level-set method. Icarus 411, 115940. http://dx.doi.org/10.1016/j.icarus.2023.115940.

Canup, R., Salmon, J., 2018. Origin of Phobos and Deimos by the impact of a Vesta-to-Ceres sized body with Mars. Sci. Adv. 4 (4), eaar6887. http://dx.doi.org/10.1126/sciadv.aar6887.

Chen, M., Yan, J., Huang, X., Zuo, Z., Willner, K., Xiang, H., Barriot, J.P., 2024. Advancements in the 3D shape reconstruction of Phobos: An analysis of shape models and future exploration directions. Astron. Astrophys. 684, A89. http://dx.doi.org/10.1051/0004-6361/202348665.

Christensen, E.J., Born, G.H., Hildebrand, C.E., Williams, B.G., 1977. The mass of Phobos from Viking flybys. Geophys. Res. Lett. 4 (12), 555–557. http://dx.doi.org/10.1029/GL004i012p00555.

Ciccarelli, E., Baresi, N., 2024. Autonomous navigation around Phobos: Applications to the Martian moons exploration mission.

Citron, R.I., Genda, H., Ida, S., 2015. Formation of Phobos and Deimos via a giant impact. Icarus 252, 334–338. http://dx.doi.org/10.1016/j.icarus.2015.02.011.

Craddock, R.A., 2011. Are Phobos and Deimos the result of a giant impact? Icarus 211 (2), 1150–1161. http://dx.doi.org/10.1016/j.icarus.2010.10.023.

DellaGiustina, D.N., Ballouz, R.L., Walsh, K.J., Marusiak, A.G., Bray, V.J., Bailey, S.H., 2024. Seismology of rubble-pile asteroids in binary systems. Mon. Not. R. Astron. Soc. 528 (4), 6568–6580. http://dx.doi.org/10.1093/mnras/stae325.

Dinsmore, J.T., de Wit, J., 2023. Constraining the interiors of asteroids through close encounters. Mon. Not. R. Astron. Soc. 520 (3), 3459–3475. http://dx.doi.org/10.1093/mnras/stac2866.

Dirkx, D., Vermeersen, L.L.A., Noomen, R., Visser, P.N.A.M., 2014. Phobos laser ranging: Numerical geodesy experiments for Martian system science. Planet. Space Sci. 99, 84–102. http://dx.doi.org/10.1016/j.pss.2014.03.022.

Dmitrovskii, A.A., Khan, A., Boehm, C., Bagheri, A., van Driel, M., 2022. Constraints on the interior structure of Phobos from tidal deformation modeling. Icarus 372, 114714. http://dx.doi.org/10.1016/j.icarus.2021.114714.

Ernst, C.M., Daly, R.T., Gaskell, R.W., Barnouin, O.S., Nair, H., Hyatt, B.A., Al Asad, M.M., Hoch, K.K.W., 2023. High-resolution shape models of Phobos and Deimos from stereophotoclinometry. Earth Planets Space 75 (1), 103. http://dx.doi.org/10.1186/s40623-023-01814-7.

Fanale, F.P., Salvail, J.R., 1990. Evolution of the water regime of Phobos. Icarus 88 (2), 380–395. http://dx.doi.org/10.1016/0019-1035(90)90089-R.

Giraud, J., Lindsay, M., Jessell, M., 2021. Generalization of level-set inversion to an arbitrary number of geologic units in a regularized least-squares framework. Geophysics 86 (4), R623–R637. http://dx.doi.org/10.1190/geo2020-0263.1.

Guo, X., Yan, J., Andert, T., Yang, X., Pätzold, M., Hahn, M., Ye, M., Liu, S., Li, F., Barriot, J.P., 2021. A lighter core for Phobos? Astron. Astrophys. 651, A110. http://dx.doi.org/10.1051/0004-6361/202038844.

Herique, A., Agnus, B., Asphaug, E., Barucci, A., Beck, P., Bellerose, J., Biele, J., Bonal, L., Bousquet, P., Bruzzone, L., Buck, C., Carnelli, I., Cheng, A., Ciarletti, V., Delbo, M., Du, J., Du, X., Eyraud, C., Fa, W., Gil Fernandez, J., Gassot, O., Granados-Alfaro, R., Green, S.F., Grieger, B., Grundmann, J.T., Grygorczuk, J., Hahnel, R., Heggy, E., Ho, T.M., Karatekin, O., Kasaba, Y., Kobayashi, T., Kofman, W., Krause, C., Kumamoto, A., Küppers, M., Laabs, M., Lange, C., Lasue, J., Levasseur-Regourd, A.C., Mallet, A., Michel, P., Mottola, S., Murdoch, N., Mütze, M., Oberst, J., Orosei, R., Plettemeier, D., Rochat, S., RodriguezSuquet, R., Rogez, Y., Schaffer, P., Snodgrass, C., Souyris, J.C., Tokarz, M., Ulamec, S., Wahlund, J.E., Zine, S., 2018. Direct observations of asteroid interior and regolith structure: Science measurement requirements. Past, Present and Future of Small Body Science and Exploration, Adv. Space Res. Past, Present and Future of Small Body Science and Exploration, 62 (8), 2141–2162.http://dx.doi.org/10.1016/j.asr.2017.10.020,

Hesselbrock, A.J., Minton, D.A., 2017. An ongoing satellite–ring cycle of Mars and the origins of Phobos and Deimos. Nat. Geosci. 10 (4), 266–269. http://dx.doi.org/10.1038/ngeo2916.

Hirata, K., Usui, T., Hyodo, R., Genda, H., Fukai, R., Lawrence, D.J., Chabot, N.L., Peplowski, P.N., Kusano, H., 2024. Mixing model of Phobos' bulk elemental composition for the determination of its origin: Multivariate analysis of MMX/MEGANE data. Icarus 410, 115891. http://dx.doi.org/10.1016/j.icarus.2023.115891.

Hu, X., Oberst, J., Willner, K., 2020. Equipotential figure of Phobos suggests its late accretion near 3.3 Mars radii. Geophys. Res. Lett. 47 (7), e2019GL085958. http://dx.doi.org/10.1029/2019GL085958.

Hunten, D.M., 1979. Capture of Phobos and Deimos by photoatmospheric drag. Icarus 37 (1), 113–123. http://dx.doi.org/10.1016/0019-1035(79)90119-2.

Hyodo, R., Genda, H., Charnoz, S., Rosenblatt, P., 2017. On the impact origin of Phobos and Deimos. I. thermodynamic and physical aspects. Astrophys. J. 845 (2), 125. http://dx.doi.org/10.3847/1538-4357/aa81c4.

Jacobson, R.A., Lainey, V., 2014. Martian satellite orbits and ephemerides. Phobos, Planet. Space Sci. Phobos, 102, 35–44.http://dx.doi.org/10.1016/j.pss.2013.06.003,

Jamet, O., Tsoulis, D., 2020. A line integral approach for the computation of the potential harmonic coefficients of a constant density polyhedron. J. Geod. 94 (3), 30.

Jekeli, C., 2007. Potential Theory and Static Gravity Field of the Earth. vol. 3, pp. 11–42. http://dx.doi.org/10.1016/B978-044452748-6.00054-7,

Kamada, A., Kuroda, T., Terada, N., Kobayashi, M., Nakagawa, H., Miyamoto, H., 2024. Modeling 4.3 Billion years of water history on Phobos. Icarus 410, 115916. http://dx.doi.org/10.1016/j.icarus.2023.115916.

Kegerreis, J.A., Lissauer, J.J., Eke, V.R., Sandnes, T.D., Elphic, R.C., 2024. Origin of Mars's moons by disruptive partial capture of an asteroid. arXiv:2407.15936.

Kofman, W., Herique, A., Barbin, Y., Barriot, J.P., Ciarletti, V., Clifford, S., Edenhofer, P., Elachi, C., Eyraud, C., Goutail, J.P., Heggy, E., Jorda, L., Lasue, J., Levasseur-Regourd, A.C., Nielsen, E., Pasquero, P., Preusker, F., Puget, P., Plettemeier, D., Rogez, Y., Sierks, H., Statz, C., Svedhem, H., Williams, I., Zine, S., Van Zyl, J., 2015. Properties of the 67P/Churyumov-Gerasimenko interior revealed by CONSERT radar. Science 349 (6247), aab0639. http://dx.doi.org/10.1126/science.aab0639.

Kolyuka, Y., Efimov, A., Kudryavtsev, S., Margorin, O., Tarasov, V., Tikhonov, V., 1990. Refinement of the gravitational constant of phobos from phobos-2 tracking data. Sov. Astron. Lett. Vol. 16, NO. 2: MAR/APR, P. 168, 1990 16, 168.

Kuramoto, K., 2024. Origin of Phobos and Deimos awaiting direct exploration. Annu. Rev. Earth Planet. Sci. 52 (1), 495–519. http://dx.doi.org/10.1146/annurev-earth-040522-110615.

Kuramoto, K., Kawakatsu, Y., Fujimoto, M., Araya, A., Barucci, M.A., Genda, H., Hirata, N., Ikeda, H., Imamura, T., Helbert, J., Kameda, S., Kobayashi, M., Kusano, H., Lawrence, D.J., Matsumoto, K., Michel, P., Miyamoto, H., Morota, T., Nakagawa, H., Nakamura, T., Ogawa, K., Otake, H., Ozaki, M., Russell, S., Sasaki, S., Sawada, H., Senshu, H., Tachibana, S., Terada, N., Ulamec, S., Usui, T., Wada, K., Watanabe, S.i., Yokota, S., 2022. Martian moons exploration MMX: Sample return mission to Phobos elucidating formation processes of habitable planets. Earth Planets Space 74 (1), 12. http://dx.doi.org/10.1186/s40623-021-01545-7.

Lainey, V., Pasewaldt, A., Robert, V., Rosenblatt, P., Jaumann, R., Oberst, J., Roatsch, T., Willner, K., Ziese, R., Thuillot, W., 2021. Mars moon ephemerides after 14 years of mars express data. Astron. Astrophys. 650, A64. http://dx.doi.org/10.1051/0004-6361/202039406.

Lambeck, K., 1979. On the orbital evolution of the Martian satellites. J. Geophys. Res.: Solid Earth 84 (B10), 5651–5658. http://dx.doi.org/10.1029/JB084iB10p05651.

Le Maistre, S., Rivoldini, A., Rosenblatt, P., 2019. Signature of Phobos' interior structure in its gravity field and libration. Icarus 321, 272–290. http://dx.doi.org/10.1016/j.icarus.2018.11.022.

Le Maistre, S., Rosenblatt, P., Rambaux, N., Castillo-Rogez, J.C., Dehant, V., Marty, J.C., 2013. Phobos interior from librations determination using Doppler and star tracker measurements. Planet. Space Sci. 85, 106–122. http://dx.doi.org/10.1016/j.pss.2013.06.015.

Li, W., Lu, W., Qian, J., Li, Y., 2017. A multiple level set method for three-dimensional inversion of magnetic data. Geophysics 82, 1–92. http://dx.doi.org/10.1190/geo2016-0530.1.

Martinelli, R., 2020. Interplanetary Geodesic Study of the MMX Project. Master's thesis. Politecnico di Torino.

Matsumoto, K., Hirata, N., Ikeda, H., Kouyama, T., Senshu, H., Yamamoto, K., Noda, H., Miyamoto, H., Araya, A., Araki, H., Kamata, S., Baresi, N., Namiki, N., 2021. MMX geodesy investigations: Science requirements and observation strategy. Earth Planets Space 73 (1), 226. http://dx.doi.org/10.1186/s40623-021-01500-6.

Murchie, S., 1999. Mars pathfinder spectral measurements of Phobos and Deimos: Comparison with previous data. J. Geophys. Res. 104, 9069–9080. http://dx.doi.org/10.1029/98JE02248.

Murchie, S.L., Thomas, P.C., Rivkin, A.S., Chabot, N.L., 2015. Phobos and Deimos. In: Michel, P., DeMeo, F.E., Bottke, W.F. (Eds.), Asteroids IV. University of Arizona Press, http://dx.doi.org/10.2458/azu_uapress_9780816532131-ch024.

Murray, C.D., Dermott, S.F., 2000. Solar System Dynamics. Cambridge University Press, Cambridge, http://dx.doi.org/10.1017/CBO9781139174817.

Pajola, M., Lazzarin, M., Dalle Ore, C.M., Cruikshank, D.P., Roush, T.L., Magrin, S., Bertini, I., La Forgia, F., Barbieri, C., 2013. Phobos as a D-type captured asteroid, spectral modeling from 0.25 to 4.0 Mm. Astrophys. J. 777, 127. http://dx.doi.org/10.1088/0004-637X/777/2/127.

Pätzold, M., Andert, T., Tyler, G., Asmar, S., Häusler, B., Tellmann, S., 2014. Phobos mass determination from the very close flyby of Mars Express in 2010. Icarus 229, 92–98. http://dx.doi.org/10.1016/j.icarus.2013.10.021.

Poggiali, G., Matsuoka, M., Barucci, M.A., Brucato, J.R., Beck, P., Fornasier, S., Doressoundiram, A., Merlin, F., Alberini, A., 2022. Phobos and Deimos surface composition: Search for spectroscopic analogues. Mon. Not. R. Astron. Soc. 516 (1), 465–476. http://dx.doi.org/10.1093/mnras/stac2226.

Rambaux, N., Castillo-Rogez, J.C., Le Maistre, S., Rosenblatt, P., 2012. Rotational motion of Phobos. Astron. Astrophys. 548, A14. http://dx.doi.org/10.1051/0004-6361/201219710.

Ramsley, K.R., Head, J.W., 2021. The origins and geological histories of Deimos and Phobos: Hypotheses and open questions. Space Sci. Rev. 217 (8), 86. http://dx.doi.org/10.1007/s11214-021-00864-1.

Rashidifard, M., Giraud, J., Lindsay, M., Jessell, M., Ogarko, V., 2021. Constraining 3D geometric gravity inversion with a 2D reflection seismic profile using a generalized level set approach: Application to the eastern Yilgarn Craton. Solid Earth 12 (10), 2387–2406. http://dx.doi.org/10.5194/se-12-2387-2021.

Rivkin, A.S., Brown, R.H., Trilling, D.E., Bell, J.F., Plassmann, J.H., 2002. Near-infrared spectrophotometry of Phobos and Deimos. Icarus 156 (1), 64–75. http://dx.doi.org/10.1006/icar.2001.6767.

Rosenblatt, P., 2011. The origin of the Martian moons revisited. Astron. Astrophys. Rev. 19 (1), 44. http://dx.doi.org/10.1007/s00159-011-0044-6.

Rosenblatt, P., Charnoz, S., Dunseath, K.M., Terao-Dunseath, M., Trinh, A., Hyodo, R., Genda, H., Toupin, S., 2016. Accretion of Phobos and Deimos in an extended debris disc stirred by transient moons. Nat. Geosci. 9 (8), 581–583. http://dx.doi.org/10.1038/ngeo2742.

Rosenblatt, P., Hyodo, R., Pignatale, F., Trinh, A., Charnoz, S., Dunseath, K., Dunseath-Terao, M., Genda, H., 2020. The formation of the Martian moons. In: Oxford Research Encyclopedia of Planetary Science. http://dx.doi.org/10.1093/acrefore/9780190647926.013.24.

Scheeres, D.J., French, A.S., Tricarico, P., Chesley, S.R., Takahashi, Y., Farnocchia, D., McMahon, J.W., Brack, D.N., Davis, A.B., Ballouz, R.L., Jawin, E.R., Rozitis, B., Emery, J.P., Ryan, A.J., Park, R.S., Rush, B.P., Mastrodemos, N., Kennedy, B.M., Bellerose, J., Lubey, D.P., Velez, D., Vaughan, A.T., Leonard, J.M., Geeraert, J., Page, B., Antreasian, P., Mazarico, E., Getzandanner, K., Rowlands, D., Moreau, M.C., Small, J., Highsmith, D.E., Goossens, S., Palmer, E.E., Weirich, J.R., Gaskell, R.W., Barnouin, O.S., Daly, M.G., Seabrook, J.A., Asad, M.M.A., Philpott, L.C., Johnson, C.L., Hartzell, C.M., Hamilton, V.E., Michel, P., Walsh, K.J., Nolan, M.C., Lauretta, D.S., 2020. Heterogeneous mass distribution of the rubble-pile asteroid (101955) Bennu. Sci. Adv. 6 (41), eabc3350. http://dx.doi.org/10.1126/sciadv.abc3350.

Takahashi, Y., Bradley, N., Kennedy, B., 2017. Determination of celestial body principal axes via gravity field estimation. J. Guid. Control Dyn. 40 (12), 3050–3060. http://dx.doi.org/10.2514/1.G002877.

Takahashi, Y., Scheeres, D.J., 2014. Morphology driven density distribution estimation for small bodies. Icarus 233, 179–193. http://dx.doi.org/10.1016/j.icarus.2014.02.004.

Tricarico, P., 2013. Global gravity inversion of bodies with arbitrary shape. Geophys. J. Int. 195 (1), 260–275. http://dx.doi.org/10.1093/gji/ggt268.

Tricarico, P., Scheeres, D.J., French, A.S., McMahon, J.W., Brack, D.N., Leonard, J.M., Antreasian, P., Chesley, S.R., Farnocchia, D., Takahashi, Y., Mazarico, E.M., Rowlands, D., Highsmith, D., Getzandanner, K., Moreau, M., Johnson, C.L., Philpott, L., Bierhaus, E.B., Walsh, K.J., Barnouin, O.S., Palmer, E.E., Weirich, J.R., Gaskell, R.W., Daly, M.G., Seabrook, J.A., Nolan, M.C., Lauretta, D.S., 2021. Internal rubble properties of asteroid (101955) Bennu. Icarus 370, 114665. http://dx.doi.org/10.1016/j.icarus.2021.114665.

Usui, T., Bajo, K.i., Fujiya, W., Furukawa, Y., Koike, M., Miura, Y.N., Sugahara, H., Tachibana, S., Takano, Y., Kuramoto, K., 2020. The importance of Phobos sample return for understanding the mars-moon system. Space Sci. Rev. 216 (4), 49. http://dx.doi.org/10.1007/s11214-020-00668-9.

Wargnier, A., Gautier, T., Poch, O., Beck, P., Quirico, E., Buch, A., Drant, T., Perrin, Z., Doressoundiram, A., 2023. Organic detection in the near-infrared spectral Phobos regolith laboratory analogue in preparation for the Martian moon exploration mission. Astronom. Astrophys 669 (January), http://dx.doi.org/10.1051/0004-6361/202245294, A146 (11p).

Willner, K., Oberst, J., Hussmann, H., Giese, B., Hoffmann, H., Matz, K.D., Roatsch, T., Duxbury, T., 2010. Phobos control point network, rotation, and shape. Mars Express after 6 Years in Orbit: Mars Geology from Three-Dimensional Mapping by the High Resolution Stereo Camera (HRSC) Experiment, Earth Planet. Sci. Lett. Mars Express after 6 Years in Orbit: Mars Geology from Three-Dimensional Mapping by the High Resolution Stereo Camera (HRSC) Experiment, 294 (3), 541–546.http://dx.doi.org/10.1016/j.epsl.2009.07.033,

Willner, K., Shi, X., Oberst, J., 2014. Phobos' shape and topography models. Phobos, Planet. Space Sci. Phobos, 102, 51–59.http://dx.doi.org/10.1016/j.pss.2013.12.006,

Yamamoto, K., Matsumoto, K., Ikeda, H., Senshu, H., Willner, K., Ziese, R., Oberst, J., 2024. Simulation of gravity field estimation of Phobos for Martian moon exploration (MMX). Earth, Planets and Space 76 (1), 86. http://dx.doi.org/10.1186/s40623-024-02017-4.

Yang, X., Yan, J.G., Andert, T., Ye, M., Pätzold, M., Hahn, M., Jin, W.T., Li, F., Barriot, J.P., 2019. The second-degree gravity coefficients of Phobos from two Mars express flybys. Mon. Not. R. Astron. Soc. 490 (2), 2007–2012. http://dx.doi.org/10.1093/mnras/stz2695.

Yoder, C.F., 1982. Tidal rigidity of phobos. Icarus 49 (3), 327–346. http://dx.doi.org/10.1016/0019-1035(82)90040-9.

Zhong, Z., Wen, Q., Yan, J., Pang, L., 2023. The mean moment of inertia for irregularly shaped Phobos and its application to the constraint for the two-layer interior structure for the Martian moon. Remote Sens. 15 (12), 3162. http://dx.doi.org/10.3390/rs15123162.